

The Observed Probability Distribution Function, Power Spectrum, and Correlation Function of the Transmitted Flux in the Ly α Forest ¹

Patrick McDonald,² Jordi Miralda-Escudé,^{2,3} Michael Rauch,⁴ Wallace L. W. Sargent,⁵ Tom A. Barlow,⁵ Renyue Cen,⁶ and Jeremiah P. Ostriker⁶

ABSTRACT

A sample of eight quasars observed at high resolution and signal-to-noise is used to determine the probability distribution function (PDF), the power spectrum, and the correlation function of the transmitted flux in the Ly α forest, in three redshift bins centered at $z = 2.41$, 3.00 , and 3.89 . All the results are presented in tabular form, with full error covariance matrices to allow for comparisons with any numerical simulations and with other data sets. The observations are compared with a numerical simulation of the Ly α forest of a Λ CDM model with $\Omega = 0.4$, known to agree with other large-scale structure observational constraints. There is excellent agreement for the PDF, if the mean transmitted flux is adjusted to match the observations. A small difference between the observed and predicted PDF is found at high fluxes and low redshift, which may be due to the uncertain effects of fitting the spectral continuum. Using the numerical simulation, we show how the flux power spectrum can be used to recover the initial power spectrum of density fluctuations. From our sample of eight quasars, we measure the amplitude of the mass power spectrum to correspond to a linear variance per unit $\ln k$ of $\Delta_{\rho}^2(k) = 0.72 \pm 0.09$ at $k = 0.04 (\text{km s}^{-1})^{-1}$ and $z = 3$, and the slope of the power spectrum near the same k to be $n_p = -2.55 \pm 0.10$ (statistical error bars). The results are statistically consistent with Croft et al. , although our value for the rms fluctuation is lower by a factor 0.75. For the Λ CDM model we use, the implied primordial slope is $n = 0.93 \pm 0.10$, and the normalization is $\sigma_8 = 0.68 + 1.16(0.95 - n) \pm 0.04$.

¹The observations were made at the W.M. Keck Observatory, which is operated as a scientific partnership between the California Institute of Technology and the University of California; it was made possible by the generous support of the W.M. Keck Foundation.

²Department of Physics and Astronomy, University of Pennsylvania, Philadelphia, PA 19104; pmcdonal,jordi@llull.physics.upenn.edu

³Alfred P. Sloan Fellow

⁴ESO, Karl-Schwarzschild-Str. 2, 85748 Garching, Germany

⁵Astronomy Department, California Institute of Technology, Pasadena, CA 91125

⁶Princeton University Observatory, Peyton Hall, Princeton, NJ 08544

Subject headings: cosmology: observations—intergalactic medium—large-scale structure of universe—quasars: absorption lines

1. INTRODUCTION

The study of the Ly α forest has been making a transition toward unification with other methods of investigating the large-scale structure of the universe. Several analytical models had proposed that the structures formed at high redshift through gravitational collapse on a range of scales and gas densities could produce the Ly α forest absorption lines (Bahcall & Salpeter 1965; Arons 1972; Rees 1986; Bond, Szalay, & Silk 1988; McGill 1990; Bi 1993; Miralda-Escudé & Rees 1993). Detailed hydrodynamical simulations of the evolution of structure in a photoionized intergalactic medium (hereafter, IGM) in cold dark matter models have shown that the basic properties of the Ly α absorption spectra (see Rauch 1998 for a review) can indeed be understood by the evolving network of sheets, filaments, and halos characteristic of gravitational dynamics in cosmology (e.g., Cen et al. 1994; Zhang, Anninos, & Norman 1995; Hernquist et al. 1996; Miralda-Escudé et al. 1996; Wadsley & Bond 1996; Zhang et al. 1997; Theuns et al. 1998). Progress with theoretical modeling of the intergalactic medium occurred at the same time as the first high resolution and signal-to-noise Ly α forest spectra from the Keck telescope’s HIRES instrument (Vogt et al. 1994) became available, and as the large transverse sizes (Bechtold et al. 1994; Dinshaw et al. 1994) and the small-scale smoothness (Smette et al. 1992, 1995) of the absorbers were discovered, which eliminated many of the alternative models.

As the results of these simulations and the effects of numerical resolution, box size and thermal evolution of the IGM are better understood, one can start measuring parameters of the theory of large-scale structure from the observations of the Ly α forest. Thus, the distribution and the mean of the transmitted flux constrain the density-temperature distribution of the ionized gas, and determine a parameter depending mainly on the baryon density and the intensity of the ionizing background (Rauch et al. 1997; Weinberg et al. 1997). The power spectrum of the Ly α forest is closely related to the power spectrum of the mass fluctuations, allowing a measurement of the amplitude of these fluctuations at high redshift which gives important constraints for large-scale structure models (Croft et al. 1998, 1999; Weinberg et al. 1999; Croft, Hu, & Davé 1999). The Doppler parameter distribution of the absorption lines can be used to measure the mean temperature at different densities (Schaye et al. 1999; Ricotti, Gnedin, & Shull 1999; Bryan & Machacek 1999), which depends on the ionization history of the IGM (Hui & Gnedin 1997).

A lot of these observational results are based on a direct measurement of the statistical properties of the transmitted flux in the Ly α forest, which is a one-dimensional random field depending on the density, temperature and velocity of the gas at every point along the line of sight. While a large body of observational data has been published following the more traditional method of

fitting the absorption as being due to discrete absorbers with Voigt profiles, the work using flux statistics was generally aimed at determining specific cosmological information and less focused on a general presentation of the observational results. In this paper, we present the first detailed tabulation of the probability distribution function, power spectrum, and correlation function of the transmitted flux using the highest quality spectra currently available, and paying special attention to the calculation of error bars. The primary focus of this paper is on a clear presentation of the observational results, in a form that is useful for comparisons with future cosmological simulations and models, as well as other observations. With this aim, the statistics that we use are intended to contain the minimum amount of complexity and theoretical prejudice. We will also compare our observational results to the numerical simulation “L10” in Miralda-Escudé et al. (1996), and discuss the cosmological implications. We demonstrate how our results can be used to measure the primordial power spectrum by a method similar to Croft et al. (1999). Our data has much better resolution, $\sim 0.1 \text{ \AA}$, so we can push the measurement of $P(k)$ down to wavelengths $\lambda \sim 1h^{-1} \text{ Mpc}$.

In §2 we describe the data and the simulation that we use. In §3 we present the results for the mean and variance of the transmitted flux and discuss their implications for cosmological parameters. In §4 we present the probability distribution function of the transmitted flux and compare it to that of the numerical simulation. In §5 we present the results for the power spectrum of the transmitted flux, and compare them to the simulation. We then discuss the implications for the primordial power spectrum of the universe, from the results on scales that are large enough to make the Ly α forest fluctuations be related to quasi-linear density fluctuations. In §6 we present the correlation function of the transmitted flux. Finally, the discussion and conclusions are given in §7. Appendix B describes the computation of the error bars. All the results in this paper are available in the website <http://www.physics.upenn.edu/~jordi/lya>. In addition to all the Tables included here, the website contains also the full error covariance matrices and other details that are too extensive to be published here.

2. THE OBSERVATIONAL DATA AND THE SIMULATION

In this section we describe the observational data set and the Ly α forest simulation that we use.

2.1. Description of the Observations

We use a set of eight quasars with spectra that are fully resolved and have high signal-to-noise ratio. Seven of our quasars (Q2343+123, Q1442+293, Q1107+485, Q1425+604, Q1422+230, Q0000-262, and Q2237-061) are the same as in Rauch et al. (1997), but we add KP 77: 1623+2653, one of the triplet of quasars described in Crotts & Fang (1998). The pixel noise is typically less than 5% of the continuum flux level, and frequently as low as 1%. The velocity resolution is 6.6

km s^{-1} (FWHM) and the spectra are binned in 0.04 \AA pixels.

Continua were fitted to the HIRES spectra using the IRAF Continuum task. Spline3 or chebycheff polynomials were used. The order of the polynomials and the number of fitting regions strongly depended on the signal-to-noise in the spectra and the redshift. As a rule of thumb, the higher the S/N ratio and the weaker the absorption, the more fitting regions were used and the higher the order of a polynomial was taken (amounting to several tens of degrees of freedom for a typical case of $S/N \sim 30$, $z = 2.5$ Ly α forest spectrum). The regions between Ly α and Ly β were cut into 2 to 4 pieces for fitting, which were re-joined after fitting to form a long spectrum.

The continua were fitted to regions of the Lyman α forest deemed 'free of absorption lines' (as judged by eye). At best this is a problematic definition, as the perception of a stretch of spectrum as being free of absorption depends on the signal-to-noise ratio of the data, the average line density (and thus the redshift), the mean background absorption (i.e., the possibility of a constant absorption trough on top of individual absorption lines), and the spectral resolution. The last point does not pose a problem for the current data as absorption features with widths down to 6.6 km s^{-1} are resolved, and typical Lyman α line widths are much larger than that (e.g., Rauch et al. 1992). The possibility of unrecognized large-scale absorption features in the absorption is a more serious concern. Determining the position and extent of line-free spectral regions by eye tends to mistake large shallow flux depressions as parts of the unabsorbed continuum, so the continuum would be systematically placed low, leading to an underestimate of the absorbed optical depth. Similar problems arise for the high redshift ($z > 4$) Ly α forest where more than half of the flux is absorbed and the spectrum 'between the absorption lines' rarely recovers enough to reach the probable continuum level of the QSO. In such cases only a stiff polynomial (typically with 3 to 5 degrees of freedom for the region from Ly α to Ly β) can be used. This lack of information caused by the sparsely sampled continuum can lead to local uncertainties in the continuum exceeding 5% , as can be shown by comparison with more easily flux-normalizeable, low resolution single order spectra of the same QSO. The S/N ratio, finally, may also lead to biases, in that, at higher redshifts, the apparently unabsorbed continuum portions between the absorption lines shrink in size and noise. As the final selection of fitting regions is done by eye, the shortness of the continuum portions could easily eliminate true continuum regions or introduce spurious ones in the sample of supposed continuum data points. This last effect does not produce global errors in the continuum level, but it can introduce local fluctuations.

These uncertainties in the continuum fitting can affect the results reported in this paper on the flux distribution function, the power spectrum and the correlation function, and should be considered as a source of possible systematic errors in addition to quoted statistical errors of the results. This underscores the need to obtain spectra in the future with a good flux calibration, so that the continuum can be fitted with many fewer free parameters under the assumption of a smooth underlying continuum spectrum of the observed quasar Press, Rybicki, & Schneider (1993).

Figure 1 shows the redshift range covered by the useful part of each spectrum. The wave-

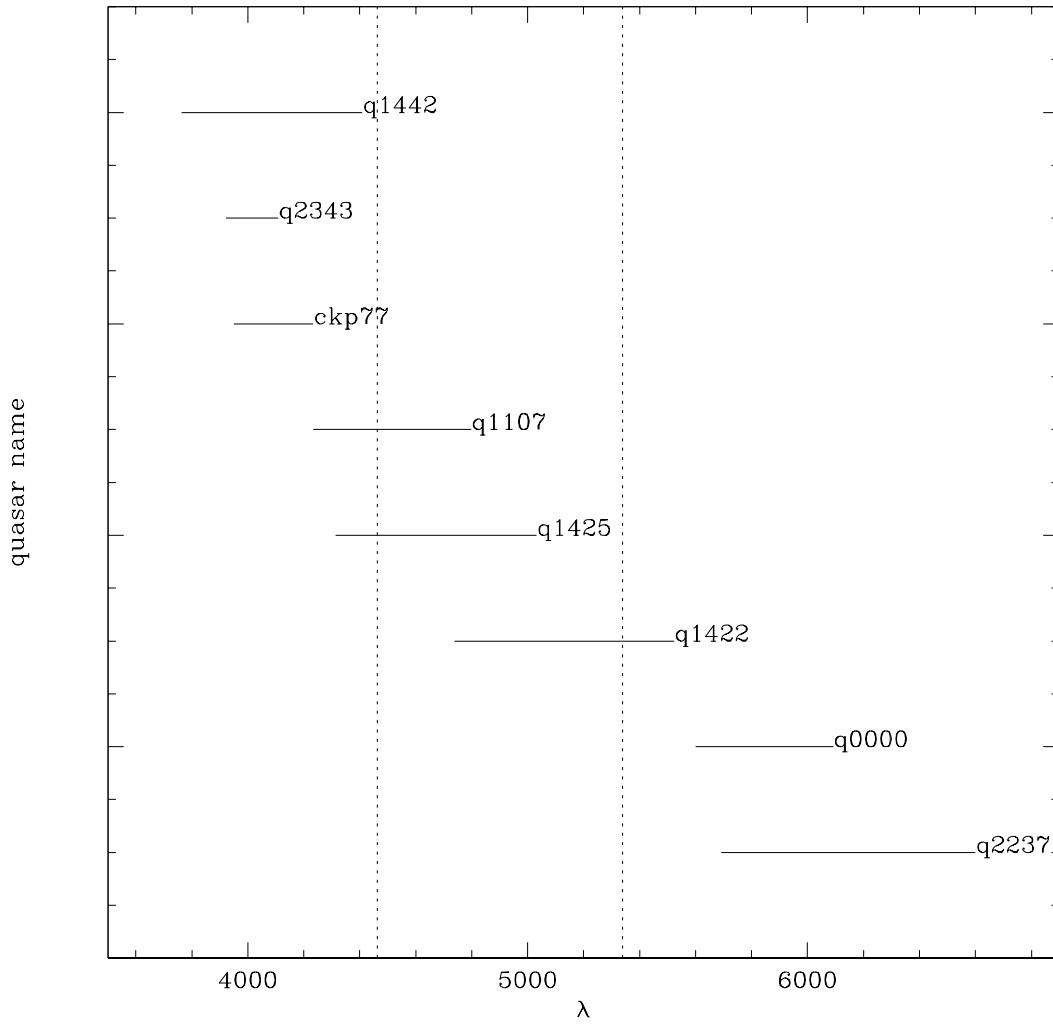


Fig. 1.— The useful redshift range covered by each quasar. The vertical axis is meaningless. The vertical dotted lines at $z = 2.67$ and $z = 3.39$ separate the data into the three redshift bins that we will use.

length regions of the spectra of these eight quasars that were included in the present analysis were selected as follows: first, only the regions between the Ly α and Ly β emission wavelengths were included, excluding also an interval within $5 h^{-1}$ Mpc of the quasar to avoid the proximity effect. Approximately half of the KP 77 spectrum has signal-to-noise ratio lower than any of the Rauch et al. (1997) data so this region was eliminated. Finally, damped Ly α absorption lines and narrow lines known or suspected to be metal lines were removed, by eliminating small intervals of the spectra containing these absorption lines from the spectra. The detailed list of wavelength intervals eliminated in each quasar is available on the website mentioned above. The data preparation is described in more detail in Rauch et al. (1997) and Barlow & Sargent (1997).

2.2. Calculation of Errors

We present in this paper the results on the flux distribution function (in greater detail than in Rauch et al. 1997), as well as the power spectrum and correlation function of the transmitted flux. All the observational results are given with error bars obtained using the bootstrap method (Press et al. 1992), including the full covariance matrices for all the results except the power spectrum. The bootstrap procedure consists of dividing the data into N segments and generating modified realizations of a statistic by randomly selecting N of the segments (with replacement). The dispersion in the bootstrap realizations approximates the error on the observed statistic. The method for computing the error bars is described in detail in Appendix B. We present only the diagonal elements of the error matrices in the tables here. The full covariance matrices can be obtained from the website mentioned above. Our intention is to allow detailed comparisons of these results with cosmological simulations and with other observational results.

2.3. Description of the Simulation

We compare the observations to the output of the Eulerian hydrodynamical simulation described in Miralda-Escudé et al. (1996) (referred to as L10 in that paper). The cosmological model used is $\Omega_0 = 0.4$, $\Omega_\Lambda = 0.6$, $h = 0.65$, $\sigma_8 = 0.79$, and a large-scale primordial power spectrum slope $n = 0.95$. This model is in agreement with the large set of observations of large-scale structure currently available (e.g., Wang et al. 1999). The box size of the simulation is $10h^{-1}$ Mpc, and it contains 288^3 cells. Ly α spectra are computed for a large number of lines of sight along the box axes. There is one free parameter that we can vary when computing the spectra, the normalization of the optical depth, which we adjust to reproduce the observed transmitted flux, as we show in §3. Renormalizing the optical depth is equivalent to modifying the intensity of the ionizing background, as long as the effect of collisional ionization and the change in the gas temperature caused by the different heating rate can be neglected (see Theuns et al. 1998 for a test that these effects are in fact negligible; notice that collisional ionization is actually important in high temperature gas in the simulations, but this gas is always at high density and produces saturated absorption in Ly α

). The optical depth is then mapped to transmitted flux using $F = \exp(-\tau)$.

These theoretical spectra are then modified to account for the continuum fitting, resolution and noise in the observations. Of these three effects, the most difficult to reproduce is the operation of continuum fitting, where several points along the spectrum of the quasars that appear not to have any obvious absorption are selected to indicate the quasar continuum. This operation is inevitable if the intrinsic spectrum of the quasar is unknown. Unfortunately, there is not really a good way to correct for it because the spectra obtained from simulations obviously have the period of the simulated box, which is comparable to the typical distance between successive continuum fitting points.

Following Rauch et al. (1997), we estimate the effects of continuum fitting by defining the maximum transmitted flux along any line of sight in the simulation (parallel to one of the three axes) to be the continuum flux, F_c , and dividing the flux in all other pixels by F_c . We convolve with the instrumental resolution of 6.6 km s^{-1} , and we add Gaussian noise to each cell with the dispersion $n(F)$, which is given below in Table 3. The dispersion $n(F)$ is computed as the mean noise in all pixels in the observed spectra for every flux bin. Notice that the noise increases with the flux value because there is a constant background noise plus the Poisson noise of the photon counts in each pixel. We also map the 288 cells along an axis in the simulation onto 512 pixels in the spectra, to facilitate the computation of Fourier transforms. The noise in Table 3 is for the pixel width in the observational data, 0.04 \AA . When we compute the power spectrum and correlation function this noise level is multiplied by $(0.04 \text{ \AA} / \Delta\lambda_{sim})^{1/2}$ where $\Delta\lambda_{sim}$ is the wavelength extent of the pixels in the simulated spectra.

In Rauch et al. (1997), an additional correction to the observed spectra was applied to correct for the redshift evolution within a redshift bin before a comparison is made with a simulation at a given redshift z_i . This consisted of multiplying the optical depth in pixels within a redshift bin around z_i by the factor $[(1+z)/(1+z_i)]^{4.5}$, so that all the observed pixels are corrected to a redshift z_i according to a law that approximately fits the observed evolution. We do not apply this correction here. The correction is small for the redshift bins we shall use; nevertheless, it must be born in mind that our observational results for the flux distribution and power spectrum are averages over each of our redshift bins. The reason we do not include this correction is that it changes the statistical distribution of the pixel noise in a way that biases some of the results. Not including the correction also makes it easier to compare to any simulation in an accurate way: after the continuum fitting, resolution and noise are included in simulated spectra, one can average the quantity being compared over the same redshift bins used here.

3. THE MEAN AND VARIANCE OF THE TRANSMITTED FLUX

In this section we present results for the mean and variance of the transmitted flux, with error bars calculated using the resampling method described in Appendix B. We then revisit the value

of Ω_b derived in Rauch et al. (1997).

The mean transmitted flux \bar{F} is computed by averaging over all the pixels in a certain data subset (either a given quasar or a redshift bin). Figure 2 shows the mean transmitted flux with error bars for each quasar. Figure 3 shows the variance of the flux for each quasar, $\sigma_F^2 = \langle (F - \bar{F})^2 \rangle - \sigma_{noise}^2$. The variance contributed by the pixel noise, σ_{noise}^2 , is generally negligible. The pixel noise does not significantly affect the error bars on the mean and variance of the transmitted flux, which are dominated by the fluctuations in the number of absorbers in the spectra. We notice that the increase of σ_F^2 with redshift is due to the increasing mean flux decrement (the true density fluctuations are of course decreasing with redshift due to gravitational clustering evolution).

The results for \bar{F} and σ_F^2 are presented in three redshift bins, centered at $\bar{z} = 2.41$, $\bar{z} = 3.00$, and $\bar{z} = 3.89$, in Table 1. Each of these bins contains about one third of the data. We will use the same redshift bins for presenting observational results in the rest of the paper. The decrease in fluctuations with increasing \bar{F} accounts for the smaller error bar on the mean transmitted flux at $\bar{z} = 2.41$.

3.1. Cosmological Implications of the Mean Flux Decrement Revisited

The value of the mean transmitted flux is related to the parameter:

$$\mu = \left(\frac{\Omega_B h^2}{0.0125} \right)^2 \left[\frac{100 \text{ km s}^{-1} \text{ Mpc}^{-1}}{H(z)} \right] \left(\frac{1}{\Gamma_{-12}} \right), \quad (1)$$

where $\Gamma = 10^{-12} \Gamma_{-12} \text{ s}^{-1}$ is the photoionization rate due to the cosmic ionizing background. The constant μ includes the simple dependences on cosmological parameters that arise from photoionization equilibrium: if the spatial distribution of the overdensity, temperature and peculiar velocity of the gas is not altered, the optical depth at every pixel is proportional to μ when Ω_b , H_0 and Γ are varied.

Table 2 presents the value of μ required for the mean transmitted flux, predicted directly from our simulation, to match the observed one, with and without the continuum fitting correction. The values are given for the same three redshift bins used before (see Table 1). We derive μ using two simulation outputs for two of the redshift bins of the observational data. We shall see in §5 that comparing the data to the simulation outputs at different redshifts is approximately equivalent to varying the amplitude of the power spectrum in the model, and that the two simulation redshifts used in Table 2 bracket the amplitude that is inferred from our data. In addition to the amplitude of the power spectrum, the simulation outputs at different redshifts also differ on the distribution of temperatures. The mean temperature at overdensity of unity is given in the last column of Table 2). The differences in the derived μ for different simulation outputs in Table 2 are due to both the different temperatures and the declining fluctuation amplitude with redshift.

The values of μ we find are very similar to those in Rauch et al. (1997); the slight differences

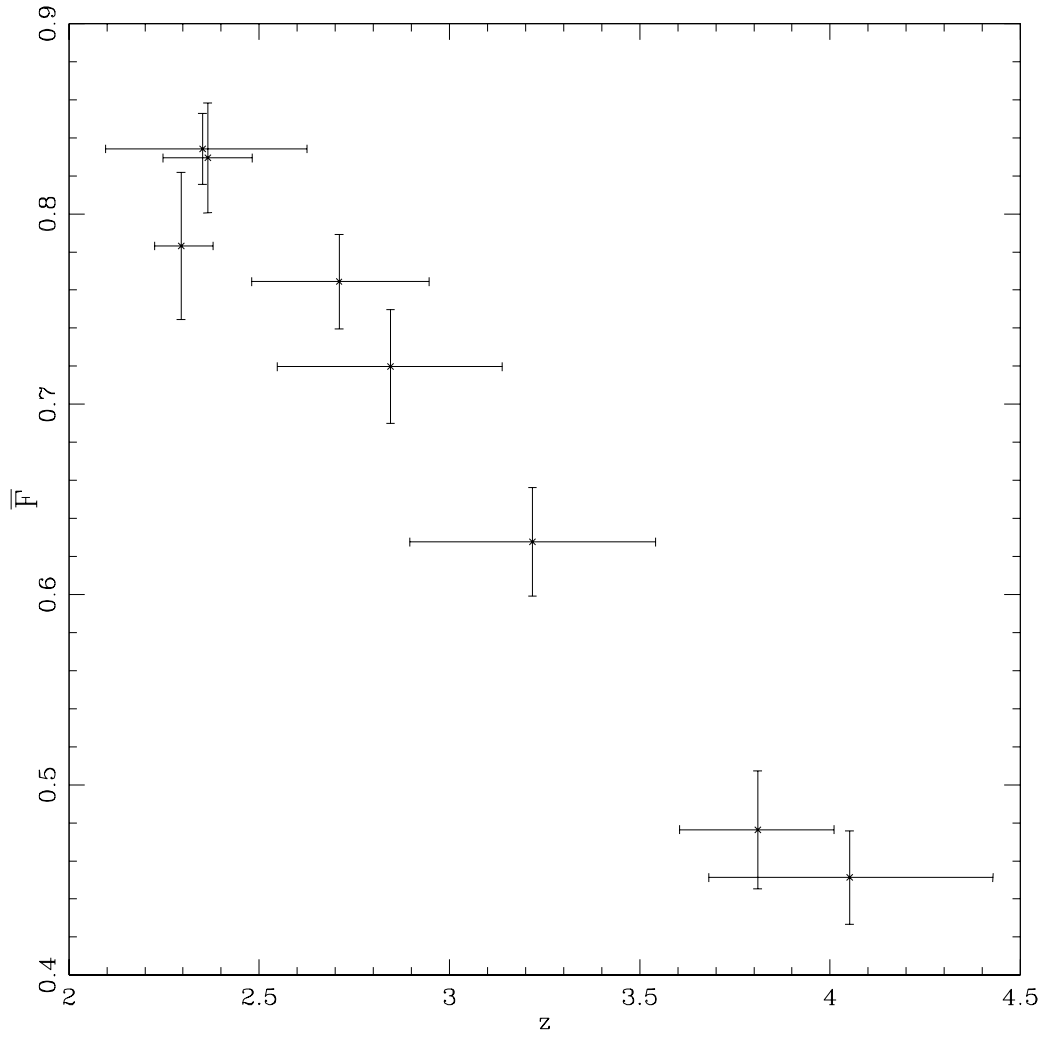


Fig. 2.— Mean transmitted flux, $\bar{F} = \langle F \rangle$, for each quasar in the sample. The error bars in the z direction show the redshift range covered by each spectrum while the point shows the mean redshift.

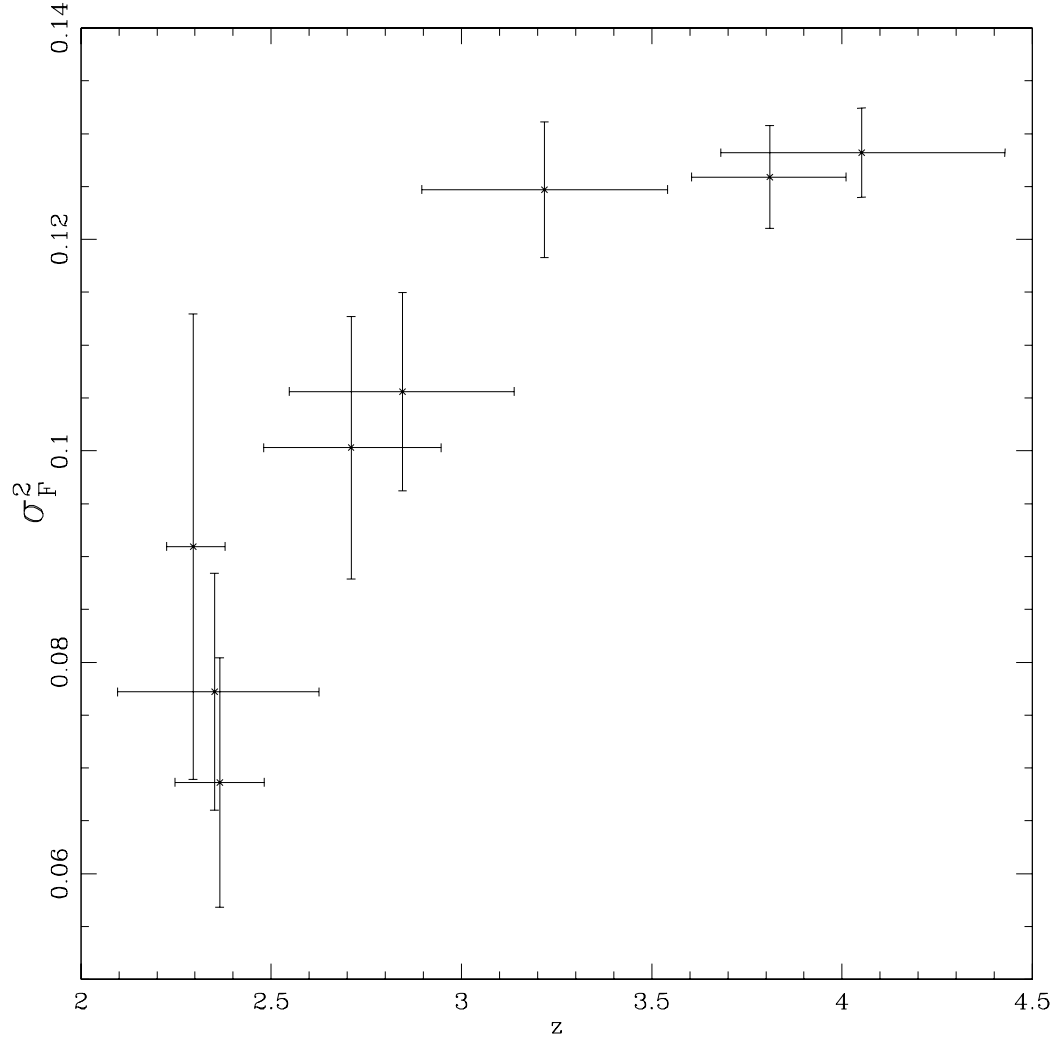


Fig. 3.— Variance of the transmitted flux, $\sigma_F^2 = \langle (F - \bar{F})^2 \rangle - \sigma_{noise}^2$, for each quasar in the sample. The error bars in the z direction show the redshift range covered by each spectrum while the point shows the mean redshift. The variance decreases with decreasing redshift because the mean transmitted flux is increasing.

Table 1. Mean and variance of the transmitted flux.

z_{min}	z_{max}	\bar{z}	\bar{F}	σ_F^2	$\langle \delta \bar{F} \delta \sigma_F^2 \rangle$	pixels
3.39	4.43	3.89	0.475 ± 0.021	0.1293 ± 0.0030	-1.0×10^{-5}	34320
2.67	3.39	3.00	0.684 ± 0.023	0.1174 ± 0.0056	-1.1×10^{-4}	31897
2.09	2.67	2.41	0.818 ± 0.012	0.0789 ± 0.0068	-7.7×10^{-5}	33791

Note. — The mean flux decrement \bar{F} , the flux variance σ_F^2 , their error correlation, and the total number of data pixels are listed for each redshift bin (z_{min}, z_{max}), with mean redshift \bar{z} .

Table 2. The optical depth normalization $\mu \propto (\Omega_b h^2)^2 (H(z) \Gamma_{-12})^{-1}$

\bar{z}_{obs}	z_{sim}	μ (cc)	μ (ncc)	Γ_{-12}	$\Omega_b h^2$	$T_{0,sim}$ (K)
2.41	2	1.58 ± 0.20	1.51 ± 0.19	0.545 ± 0.070	0.0257 ± 0.0017	13100
2.41	3	1.36 ± 0.17	1.30 ± 0.16	0.630 ± 0.082	0.0239 ± 0.0016	16000
3.00	3	1.66 ± 0.28	1.51 ± 0.23	0.412 ± 0.068	0.0296 ± 0.0024	16000
3.00	4	1.34 ± 0.21	1.20 ± 0.18	0.514 ± 0.082	0.0266 ± 0.0021	14100
3.89	4	1.44 ± 0.17	1.19 ± 0.13	0.356 ± 0.043	0.0319 ± 0.0019	14100

Note. — Computed for the observational redshift bin z_{obs} by comparison to the simulation at z_{sim} , with (cc) and without (ncc) the continuum correction. We give Γ_{-12} assuming $\Omega_b h^2 = 0.019$, and $\Omega_b h^2$ is given assuming $\Gamma_{-12} = 1$, both including the continuum correction. The median temperature at the mean density for the appropriate simulation output is given as $T_{0,sim}$.

we find when comparing to the same simulation output are due to the inclusion of a new quasar in our sample, the different choice of redshift intervals, and differences in the method of analysis (such as not including the redshift correction to the center of each redshift bin). We give also in Table 2 the statistical error bars due to the sample variance. In addition, we show the value of $\Omega_b h^2$ when $\Gamma_{-12} = 1$, and the value of Γ_{-12} when $\Omega_b h^2 = 0.019$, fixing $H(z)$ to the model $h = 0.65$, $\Omega_0 = 0.4$, $\Lambda_0 = 0.6$. We recall here that the observed abundance of quasars provides a lower limit $\Gamma_{-12} \gtrsim 1$ at $z = 3$, and therefore a corresponding lower limit to $\Omega_b h^2$, which is a bit high compared to the value derived from nucleosynthesis and the deuterium abundance of Burles & Tytler (1998) (see Rauch et al. 1997; Weinberg et al. 1997).

In addition to the μ parameter, how should the predicted mean transmitted flux depend on the specific large-scale structure model that is assumed? As we shall discuss later in §7, the dominant dependence should be on the gas temperature-density relation, and the density fluctuation amplitude at the Jeans scale (Hui & Gnedin 1997; Nusser & Haehnelt 1999see, e.g.,). Rescaling the gas temperature T_0 at a fixed overdensity will result in a variation $\mu \propto T_0^{0.7}$ for a fixed mean transmitted flux, owing to the variation of the recombination coefficient with temperature. Changing the temperature will also change the distribution of absorption, for a fixed real space distribution of gas, by altering the thermal broadening. In general, increasing the thermal broadening will increase the amount of absorption and so decrease μ for a fixed mean flux decrement. The full dependence on the gas temperature (which is affected by radiative cooling, shock heating, etc.) is more complicated; however, these two effects incorporate most of the temperature dependence.

The fluctuation amplitude at the Jeans scale in the simulation we use is probably close to the correct value in our Universe given the good agreement we find later (§4 and 5) in the transmitted flux distribution function and the power spectrum. This limits the model uncertainty in the value of μ derived from the simulation we use. However, the dependence on the density distribution is strong because the density of neutral gas is proportional to the square of the baryon density.

The different values of μ derived from different redshift outputs give an idea of the importance of the model dependence on the gas temperature and the power spectrum amplitude. A more detailed analysis using simulations where these parameters are varied will be necessary to assess the errors due to the theoretical model uncertainty on the value of μ .

4. THE PROBABILITY DISTRIBUTION OF THE TRANSMITTED FLUX

We present here the probability distribution function (hereafter, PDF) of the transmitted flux, first used as a tool to study the Ly α forest by Jenkins & Ostriker (1991). The PDF of the same observations used here (except for our addition of an eighth quasar in the sample) was presented before in Rauch et al. (1997). The results will be given here in differential form and with error bars computed as described in Appendix A. The PDF was measured from the observations with all pixels weighted equally. Table 3 gives $P(F)$ and the noise amplitude $n(F)$, which is necessary

Table 3. The observed probability distribution of the transmitted flux.

F	$P(F)$ ($z = 3.89$)	$n(F)$	$P(F)$ ($z = 3.00$)	$n(F)$	$P(F)$ ($z = 2.41$)	$n(F)$
0.00	3.618 ± 0.288	0.024	2.032 ± 0.229	0.0064	0.744 ± 0.129	0.017
0.05	1.472 ± 0.103	0.027	0.463 ± 0.043	0.0072	0.327 ± 0.043	0.022
0.10	0.666 ± 0.049	0.026	0.340 ± 0.036	0.0077	0.214 ± 0.025	0.022
0.15	0.528 ± 0.037	0.027	0.300 ± 0.028	0.0081	0.180 ± 0.020	0.021
0.20	0.524 ± 0.040	0.027	0.279 ± 0.027	0.0086	0.176 ± 0.019	0.022
0.25	0.536 ± 0.040	0.027	0.315 ± 0.034	0.0086	0.195 ± 0.020	0.022
0.30	0.546 ± 0.039	0.027	0.297 ± 0.027	0.0088	0.206 ± 0.020	0.023
0.35	0.534 ± 0.039	0.027	0.322 ± 0.030	0.0095	0.189 ± 0.020	0.024
0.40	0.571 ± 0.036	0.028	0.319 ± 0.027	0.0099	0.212 ± 0.023	0.023
0.45	0.549 ± 0.038	0.029	0.351 ± 0.028	0.0102	0.213 ± 0.020	0.025
0.50	0.598 ± 0.038	0.030	0.372 ± 0.031	0.0099	0.249 ± 0.023	0.025
0.55	0.623 ± 0.043	0.030	0.448 ± 0.041	0.0101	0.267 ± 0.024	0.025
0.60	0.706 ± 0.048	0.031	0.494 ± 0.038	0.0104	0.277 ± 0.024	0.025
0.65	0.776 ± 0.051	0.031	0.584 ± 0.043	0.0107	0.354 ± 0.029	0.027
0.70	0.856 ± 0.056	0.031	0.688 ± 0.044	0.0114	0.381 ± 0.028	0.026
0.75	0.973 ± 0.060	0.032	0.831 ± 0.059	0.0118	0.566 ± 0.038	0.028
0.80	1.119 ± 0.071	0.032	1.067 ± 0.069	0.0117	0.774 ± 0.050	0.027
0.85	1.235 ± 0.081	0.032	1.570 ± 0.094	0.0121	1.231 ± 0.063	0.029
0.90	1.302 ± 0.095	0.032	2.180 ± 0.135	0.0127	2.288 ± 0.097	0.030
0.95	1.200 ± 0.107	0.032	3.355 ± 0.169	0.0130	4.480 ± 0.143	0.029
1.00	1.068 ± 0.128	0.032	3.392 ± 0.248	0.0138	6.477 ± 0.256	0.031

Note. — The flux PDF, $P(F)$, and the average rms noise per pixel, $n(F)$, are averaged over bins covering the flux range within $\Delta F = \pm 0.025$ of the listed value of F . The first and last bins include the few additional points with $F < -0.025$ and $F > 1.025$, respectively.

for comparisons with theory. We define $n(F)$ to be the average of σ_i over all the pixels in each flux bin, where σ_i is the noise in each pixel. The noise increases with increasing F (note that the $z = 3$ data has significantly less noise than the other two redshift bins). We use 21 bins of width $\Delta F = 0.05$ with the first centered on $F = 0$ and the last on $F = 1$. Pixels with flux greater (less) than $F = 1.025$ ($F = -0.025$) are included in the last (first) bin. We provide statistical error bars on the probabilities to facilitate comparisons with theory but it is important to recognize that these error bars are significantly correlated. If a χ^2 statistic is computed from only these diagonal elements of the error matrix the distribution will be approximately twice as wide as the distribution of χ^2 properly computed from the full error matrix. The error matrix is available in the website quoted in the introduction.

Figures 4(a,b,c) show the PDF of the observations and the simulation. The mean transmitted flux in the simulation is matched to the observed mean. We compute a χ^2 statistic (using the full error matrix) to compare the observations and simulation. The results are $\chi^2/\nu = 1.1$ (with $\nu = 19$, 39% likelihood) for $z = 3.89$, $\chi^2/\nu = 1.7$ (3% likelihood) for $z = 3$, and $\chi^2/\nu = 4.4$ (negligible likelihood) for $z = 2.41$. Figures 4(a,b,c) show the effect of our continuum fitting approximation on the simulated PDF. This correction is important to the agreement seen in the two higher redshift comparisons.

The almost perfect agreement of the predicted flux distribution in the simulation and the observed distribution is impressive, and is one of the strong pieces of evidence in favor of the new Ly α forest theory based on gravitational evolution of primordial fluctuations. We believe that even the small disagreement between the simulation and observations at $\bar{z} = 2.41$ (Figure 4(a)) is due primarily to the imperfection of our continuum fitting approximation. Since the inclusion of the continuum fitting correction moves the predicted PDF in the direction of the observed one, as seen in Figure 4, it is plausible that the small remaining discrepancy is due to an underestimate of this correction. We have examined other possible reasons for this discrepancy, and they were all found to be not significant. One of these is that the noise that we include in the simulations (assumed to have a Gaussian distribution for a given flux F , obtained from the average of the variance of all pixels with flux F in Table 3) does not adequately represent the true distribution function of the noise, which is actually a sum of Gaussians with the variance distribution of all the pixels with flux F in the observations. We tested this by computing the predicted $P(F)$ given the actual distribution of noise, and found that the difference it makes is much smaller than the differences between prediction and observation at $\bar{z} = 2.41$. Thus, the average noise values we give in Table 3 should be sufficient to compare results of any other numerical simulations with the observational data presented here on $P(F)$. Another effect is that observational results are obtained by averaging over a certain redshift interval, whereas the simulation predictions are for a fixed redshift. The importance of this effect was tested by creating sets of spectra where each line of sight had a different value for μ , given by $\mu = \mu_0 [(1+z)/(1+\bar{z})]^{4.5}$, where μ_0 is the value of μ at the mean redshift and z is varied across the full width of the redshift bin in the observational data; there was negligible change in the predicted PDF of the flux.

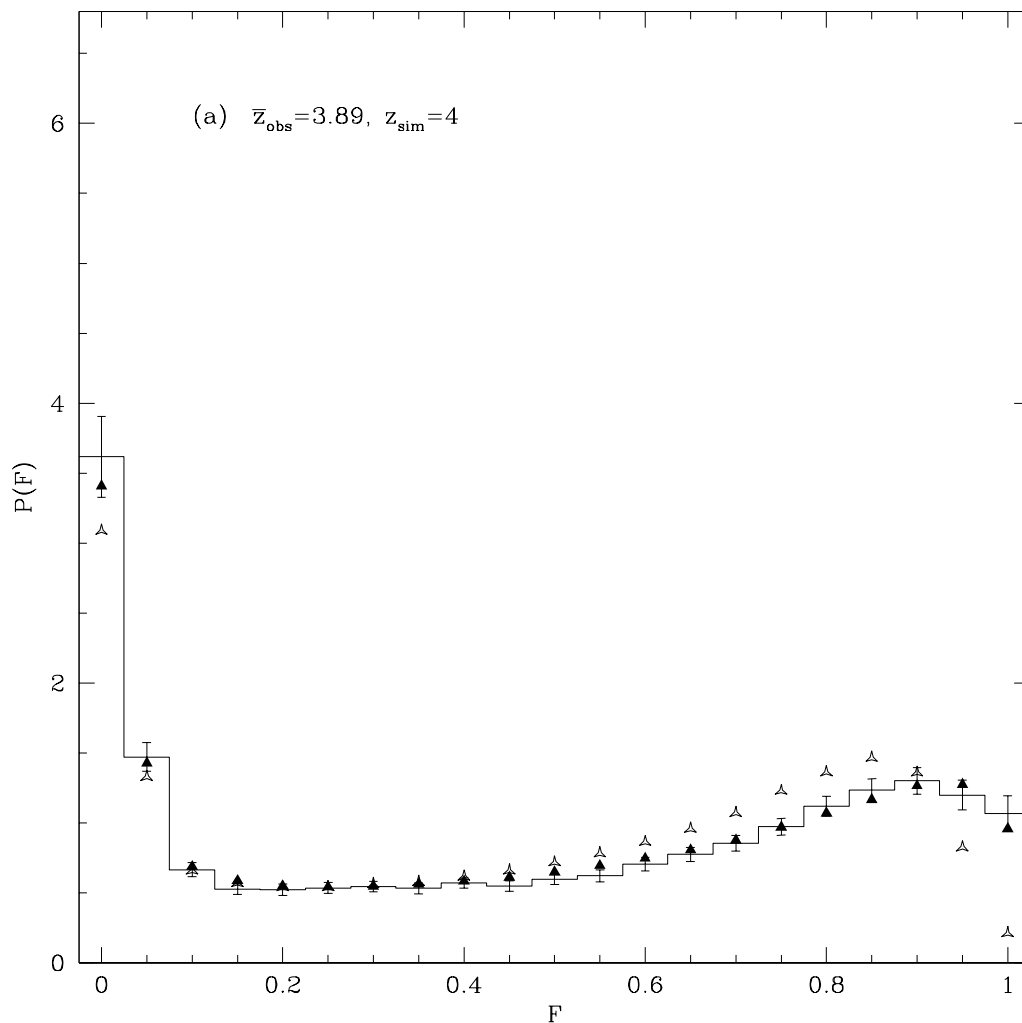
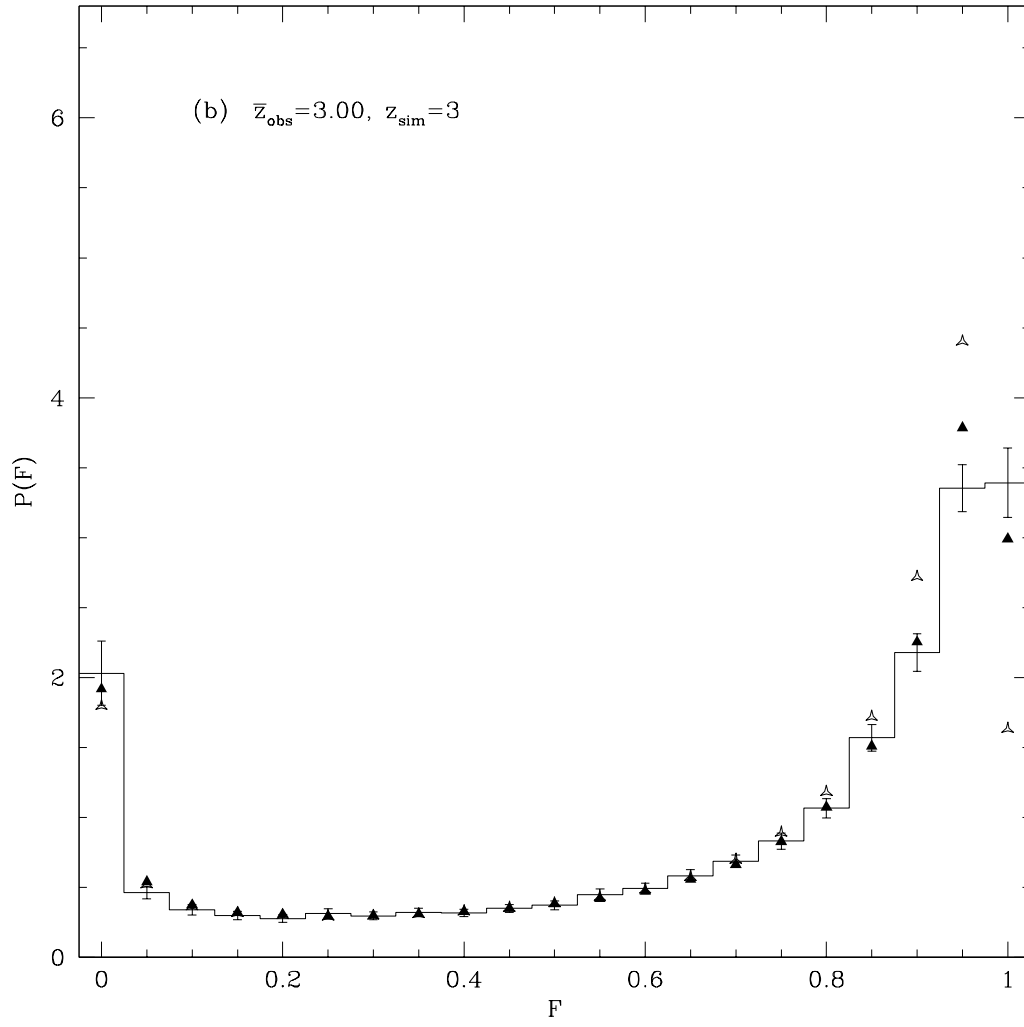
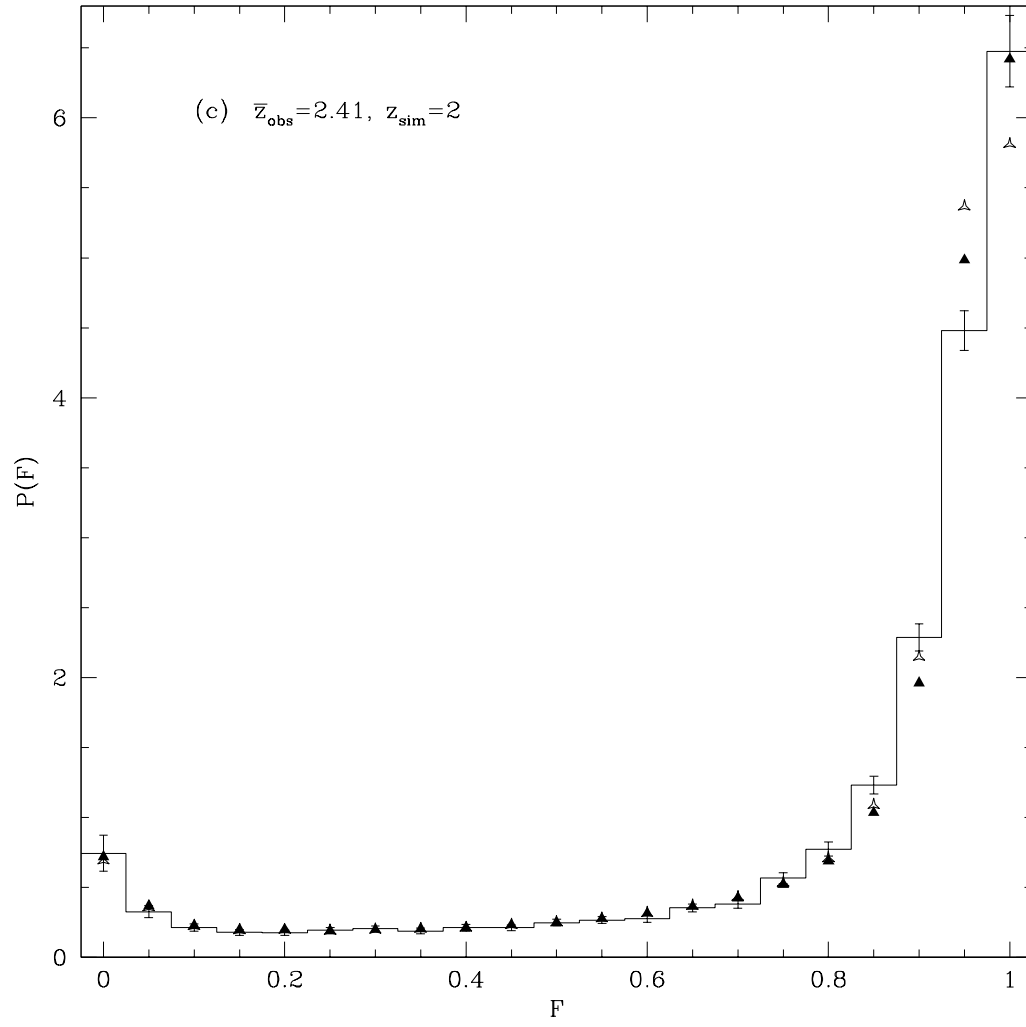


Fig. 4.— The PDF of F for the observations (*histograms*) and for the simulation with the continuum fitting approximation (*filled points*) and without it (*open points*). The small number of points outside the displayed range of F are included in the outermost bins. Errors bars were generated by bootstrap resampling. The numerical simulation has \bar{F} fixed to agree with the observations. (a) shows $\bar{z} = 3.89$, (b) shows $\bar{z} = 3.00$, and (c) shows $\bar{z} = 2.41$.





Why is there such a good agreement between the predicted $P(F)$ and the observed one, after having adjusted only one parameter (the mean transmitted flux)? To understand the significance of this result, it is useful to think of the optical depth on a given pixel as being determined mostly by the gas density and temperature at a given point in space, $\tau \propto \rho^2 T^{-0.7}$ (from photoionization equilibrium). Given a $\rho - T$ relation determined by the photoionization history (Hui & Gnedin 1997), the predicted $P(F)$ should essentially be a result of gravitational evolution starting from Gaussian initial conditions, and it should mostly depend on one parameter only (in addition to the mean transmitted flux): the amplitude of fluctuations on the Jeans scale. Obviously, the higher the amplitude of density fluctuations, the larger the dispersion in the transmitted flux should be. A weaker dependence on the $\rho - T$ relation can also be expected. This suggests two possible implications of the good agreement of the prediction of $P(F)$ with the observations, which will need to be examined further: (a) the Ly α forest is indeed a result of gravitational evolution in a photoionized IGM starting from Gaussian initial conditions; (b) the amplitude of fluctuations in the Λ CDM model assumed in the simulation is close to the true value in the universe.

In the next Section, our analysis of the power spectrum will show that the amplitude of fluctuations in the simulation we use should actually be reduced by $\sim 15\%$ to match the observations. However, the finite size of the simulated box reduces the effective power, resulting by chance in a value of the variance of the transmitted flux that matches very well the observations (see §6).

5. THE POWER SPECTRUM

In this section we compute the one dimensional power spectrum of the transmitted flux, $P_F(k)$. The flux power spectrum is the most straightforward two-point statistic that can be measured from the data. Hopefully this will make the results more generally useful for comparisons with analytic theory, numerical simulations, and other observations. We shall then study the relation of the flux power spectrum to the linear mass power spectrum using the numerical simulation, on scales that are large enough to make the fluctuations in Ly α absorption be related to linear density fluctuations. This relation in the large-scale limit is further discussed in Appendix C. Although there are theoretical reasons to Gaussianize the transmitted flux before obtaining the power spectrum (Croft et al. 1998) this operation can amplify the effect of the noise, and its merit in improving the recovery of the linear power spectrum has not been made clear.

The data is given in the form of pixels with wavelength label λ_i and flux value F_i . We measure distance between pixels in units of the local velocity scale using the formula

$$\Delta v_i = \frac{H(\bar{z})}{1 + \bar{z}} \Delta r_i = \frac{H(\bar{z})}{1 + \bar{z}} \int_{\bar{z}}^{z_i} \frac{c dz'}{H(z')} = 2c \left(1 - \sqrt{\frac{\bar{\lambda}}{\lambda_i}} \right), \quad (2)$$

where $\bar{\lambda} = \lambda_\alpha(1 + \bar{z})$ is the wavelength at the mean redshift, \bar{z} , of any given data subset, and Δr_i is the comoving distance between pixel i and a pixel at the mean redshift, where we have

assumed an Einstein-de Sitter universe for this calculation. With this formula, separations are precisely proportional to comoving distance for an Einstein-de Sitter universe, and are a close enough approximation for other cosmologies for the redshifts intervals we shall use. The power spectrum is then estimated from each spectrum using the Lomb periodogram code in Press et al. (1992). This algorithm is designed for use on unevenly sampled data (the uneven sampling in our case is due to the removal of the chunks in the spectra containing damped Ly α and metal lines, and to the change in pixel size with redshift), and avoids rebinning of the data. The computed modes are averaged over bins evenly spaced in $\log(k)$.

5.1. Results for the Observed $P_F(k)$

Table 4 lists the results of the flux power spectrum measurements from the observational data, over the range $0.0025 (\text{km s}^{-1})^{-1} < k < 0.16(\text{km s}^{-1})^{-1}$ (the power at $k < 0.0025(\text{km s}^{-1})^{-1}$ is possibly distorted by the continuum fitting operation, and at $k > 0.16(\text{km s}^{-1})^{-1}$ the power is strongly affected by narrow metal lines and other systematic errors that are discussed below). Note that the velocity scales represent different comoving scales at each of the three redshifts. The error bars were determined as described in Appendix B; for the power spectrum they are approximately independent (as expected in linear theory). Our normalization convention is that the rms flux fluctuation is $\sigma_F^2 = \int_{-\infty}^{\infty} (dk/2\pi) P_F(k)$.

The observed $P_F(k)$ is plotted in Figures 5(a,b,c) (crosses with error bars) for the three usual redshift bins. Notice that we plot the quantity $k P_F(k)$, for easier visualization. We also plot the power spectrum measured from the simulation (solid line), with the mean flux decrement adjusted to match the observation in every redshift interval. There is generally very good qualitative agreement between the simulations and observations on large scales ($k \lesssim 0.1(\text{km s}^{-1})^{-1}$). On small scales ($k \gtrsim 0.3(\text{km s}^{-1})^{-1}$), the simulated power spectrum is constant due to the noise that we add, matching that in the observations. The different behavior of the observed $P_F(k)$ is due to various effects that we shall now describe.

The measurement of the power spectrum is complicated by the possible presence of metal lines in the spectra. Because the metal lines are narrower than the Ly α forest lines, they can affect the power spectrum on very small scales. The numbers listed in Table 4, shown as crosses in Figure 5, exclude potentially contaminated regions, but some of these regions might contain genuine Ly α lines that were selectively eliminated as suspected metal lines because they are narrow. The solid triangles in Figure 5 show the power spectrum with these regions included (except for a few regions that contain damped Ly α systems or bad data points). We see that the suspected metal lines are significant in adding small scale power. This problem in the determination of the power spectrum occurs on the smallest scales only (starting with the fifteenth bin in Table 4).

The removal of chunks of spectra suspected of containing metal lines changes the effective window function for the power spectrum measurement. To show the magnitude of this effect, we

Table 4. The observed power spectrum of the flux.

$k_{bin,min}$ ([km s ⁻¹] ⁻¹)	k_{mean} ([km s ⁻¹] ⁻¹)	$P_F(k)$ ($\bar{z} = 3.89$) (km s ⁻¹)	$P_F(k)$ ($\bar{z} = 3.00$) (km s ⁻¹)	$P_F(k)$ ($\bar{z} = 2.41$) (km s ⁻¹)
0.00251	0.00284	17.1 ± 2.8	20.8 ± 3.9	9.17 ± 2.6
0.00316	0.00358	12 ± 4	16.1 ± 4	9.68 ± 2.6
0.00398	0.0045	18.9 ± 3.3	14.7 ± 2.8	13.3 ± 3.4
0.00501	0.00566	17.5 ± 4.7	22.7 ± 4.7	11.4 ± 2.2
0.00631	0.00713	16.9 ± 3.1	10.8 ± 1.6	11.4 ± 1.9
0.00795	0.00898	15.4 ± 2.4	10.1 ± 1.7	10.2 ± 0.95
0.01	0.0113	9.44 ± 1.1	9.08 ± 1.9	7.5 ± 1.6
0.0126	0.0142	8.26 ± 1.4	8.07 ± 1	5.95 ± 0.9
0.0159	0.0179	8.15 ± 1.1	5.61 ± 0.35	4.11 ± 0.5
0.02	0.0225	4.88 ± 0.57	4.96 ± 0.7	3.58 ± 0.35
0.0251	0.0284	4.12 ± 0.34	3.59 ± 0.43	2.5 ± 0.31
0.0316	0.0357	3.03 ± 0.3	2.11 ± 0.3	1.49 ± 0.16
0.0398	0.045	1.94 ± 0.24	1.53 ± 0.14	1.05 ± 0.077
0.0501	0.0566	1.12 ± 0.15	0.896 ± 0.094	0.555 ± 0.038
0.0631	0.0713	0.629 ± 0.049	0.435 ± 0.051	0.28 ± 0.02
0.0795	0.0898	0.349 ± 0.033	0.188 ± 0.016	0.136 ± 0.014
0.1	0.113	0.141 ± 0.013	0.0691 ± 0.007	0.0473 ± 0.0044
0.126	0.142	0.0499 ± 0.0041	0.0208 ± 0.0022	0.0217 ± 0.0025

Note. — Averaged over bins defined by the listed values of k_{min} [the maximum k for the final bin is $k_{max} = 0.159$ (km s⁻¹)⁻¹], with average k value k_{mean} .

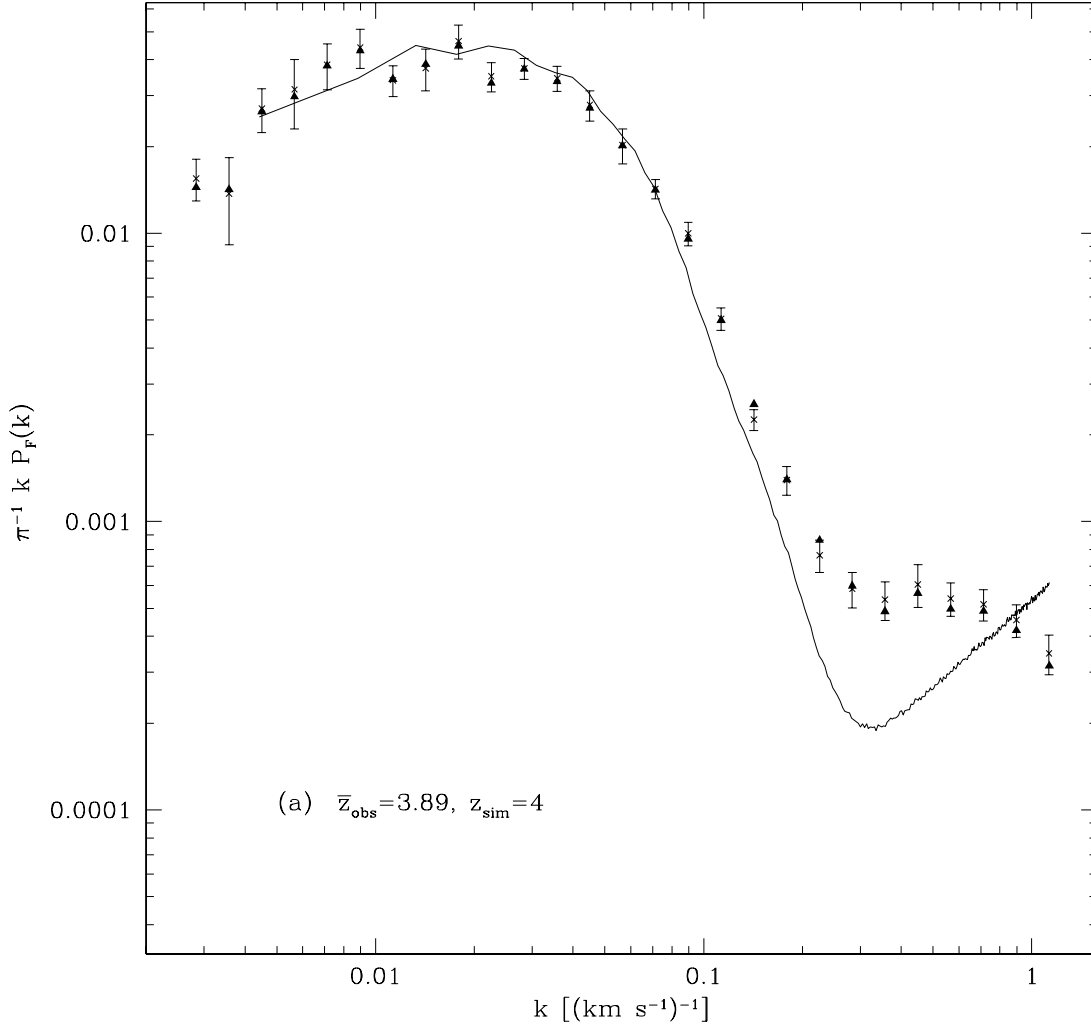
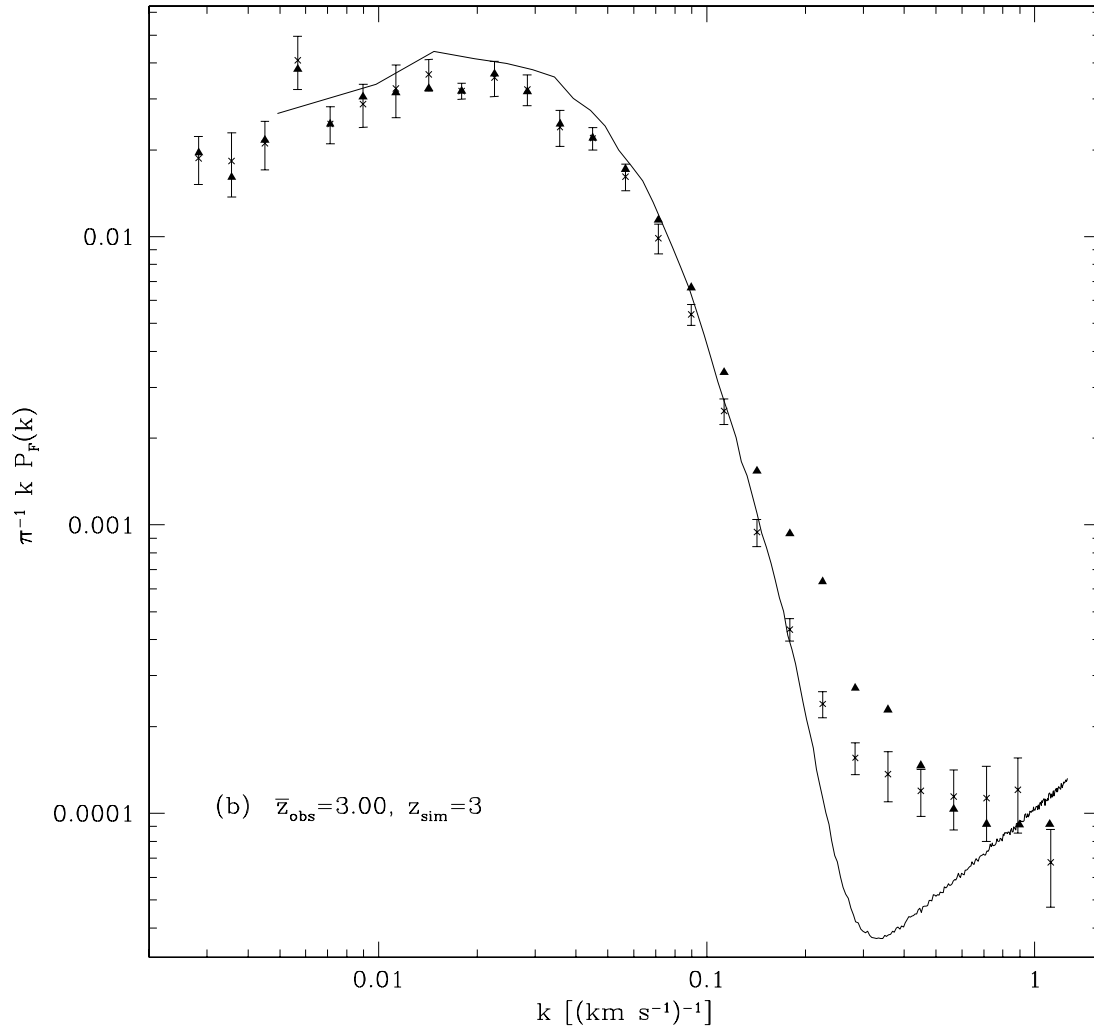
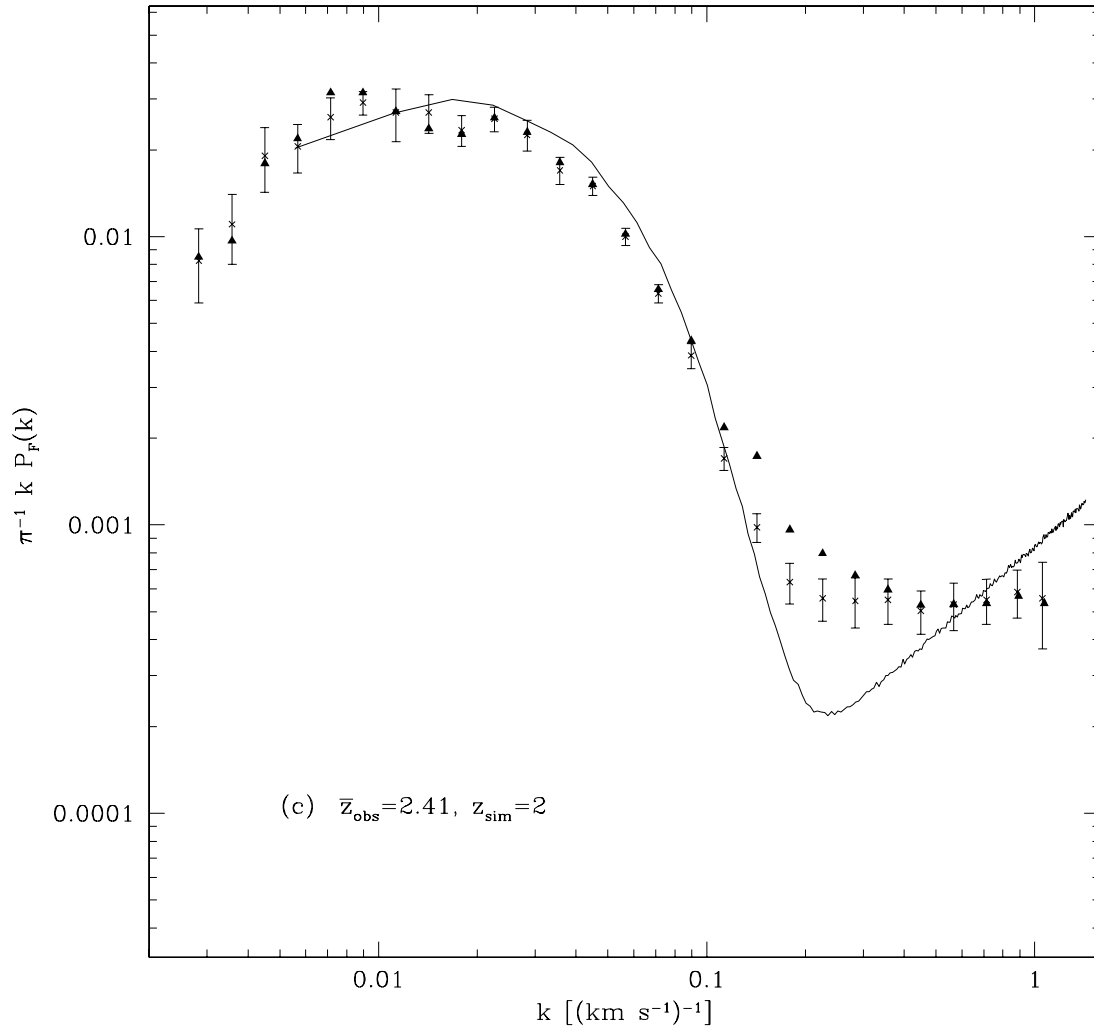


Fig. 5.— The observed one dimensional power spectra computed with and without including the regions possibly contaminated by metal lines. The points with error bars show $P_F(k)$ computed after excluding the possibly contaminated regions while the triangles show the points computed from the complete spectra. The solid lines show the power spectra from the simulation with the mean transmitted flux adjusted to match the observations. (a) shows $\bar{z} = 3.89$, (b) shows $\bar{z} = 3.00$, and (c) shows $\bar{z} = 2.41$.





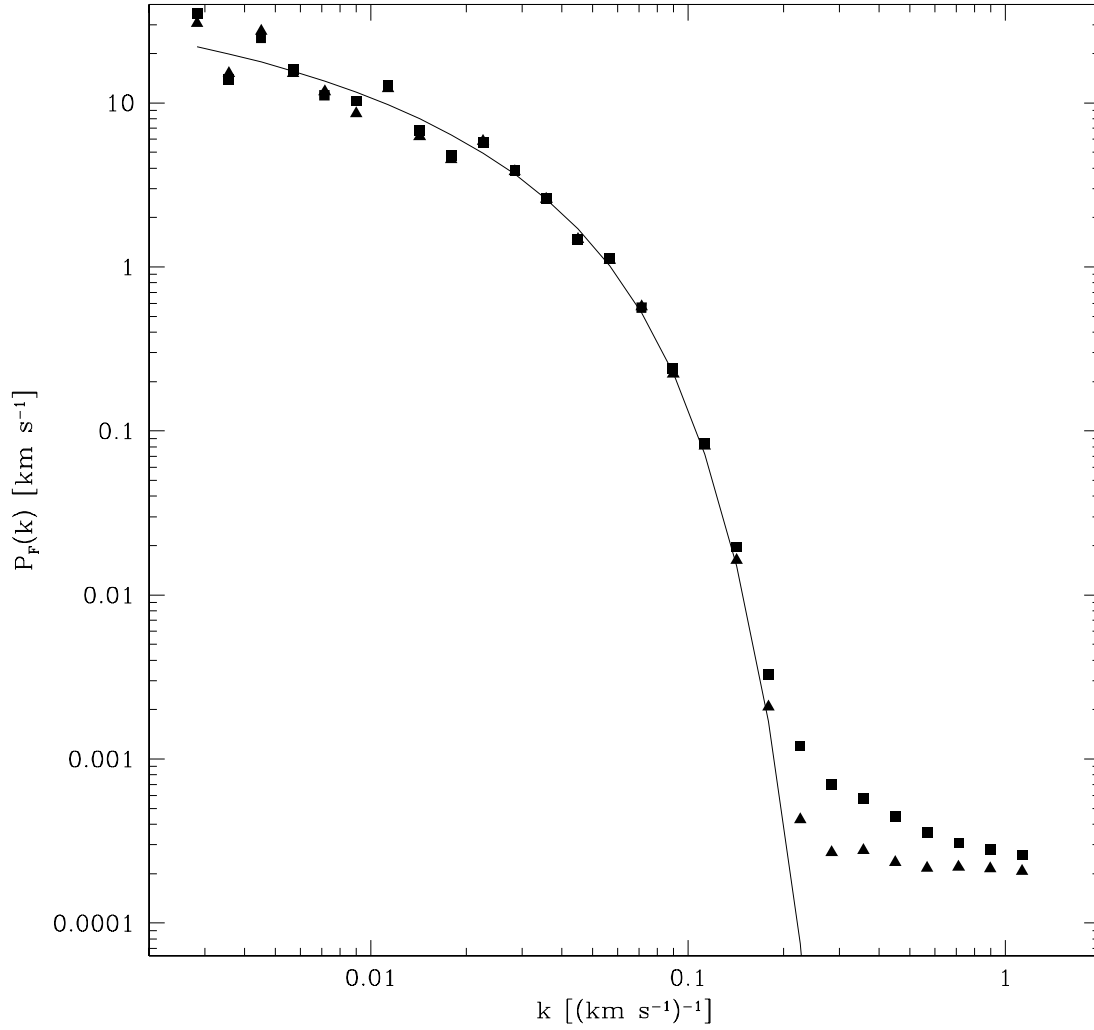


Fig. 6.— The power spectrum measured from randomly generated spectra with input power spectrum shown by the solid curve (see Appendix A). The triangles show the power measured from the full spectrum, while the squares show the power measured after the regions that are suspect in the real data are removed. The power is increased on the smallest scales when the window function is modified by removing the chunks. Figure 5 shows the opposite effect because the removed regions in the real data contain narrow lines. The flattening of both sets of points on the smallest scales is because of the noise added to the random spectra.

have randomly generated Gaussian spectra with the one-dimensional, linear power spectrum shown by the solid line in Figure 6, with a total length in velocity equal to the size of the observational sample used here in each redshift interval. The procedure we have used for generating these mock spectra is described in detail in Appendix A. We have then measured the power spectrum with the same method used for the observations, with and without removing the same chunks of the spectra that contain metal lines in the real observations. The measured $P_F(k)$ points for the case where the chunks are not removed (solid triangles) appear to follow the input power spectrum (except for statistical fluctuations at small k), until the power is small enough that the added noise begins to dominate. When the chunks are removed (solid squares), the change in the window function results in increased power on small scales. In the observational data the removed chunks contain narrow lines which have a greater effect on the power spectrum than the change in the window function, so the power decreases when the chunks are removed, except for $z_{obs} = 3.89$ where the two effects approximately cancel.

In the rest of §5, we do a quantitative comparison of the observed and simulated power spectrum. We will not use the measurements on small scales where the effects of the metal lines and the window function are important.

5.2. Fitting Formula for $P_F(k)$

The mass power spectrum of the linear density perturbations for cold dark matter models can be fitted by the form

$$P_{3D}(q) = A \frac{q^n [\ln(1 + \alpha_1 q) / \alpha_1 q]^2}{[1 + \alpha_2 q + (\alpha_3 q)^2 + (\alpha_4 q)^3 + (\alpha_5 q)^4]^{\frac{1}{2}}}, \quad (3)$$

where $q \equiv k/\Gamma(z)$, $\Gamma(z) = (1+z)\Omega_0 h^2/H(z)$ (when k has units of inverse velocity), and A is a normalization constant. The subscript 3D is written here to remind us that this is the power spectrum for fluctuations in three-dimensional real space. The formula is given by Bardeen et al. (1986), but we modify the parameters to the fit for $\Omega_b = 0.05$: $\alpha_1 = 2.205$, $\alpha_2 = 4.05$, $\alpha_3 = 18.3$, $\alpha_4 = 8.725$, and $\alpha_5 = 8.0$ (Ma 1996). The amplitude parameter A has units of $(\text{km s}^{-1})^3$. For the initial conditions of our simulation, $n = 0.95$, $\Gamma(z)$ can be found using $\Omega_0 = 0.4$, $\Omega_\Lambda = 0.6$, and $h = 0.65$, and then A can be found from $\sigma_8 = 0.79$.

Croft et al. (1998) found that multiplying the three dimensional linear theory power spectrum by the smoothing function $\exp(-k^2 w_c^2)$, with $w_c \simeq 34 \text{ km s}^{-1}$ at $z = 3$, matches the Ly α forest power spectrum obtained in their simulations. We also find that this function fits the output of our simulation reasonably well down to remarkably small scales, although we obtain smaller values of the 3D Gaussian cutoff: $w_c \simeq 12 \text{ km s}^{-1}$. It seems probable that, as Croft et al. (1999) speculated, the high w_c found by Croft et al. (1998) is a result of their lower simulation resolution. Their mean particle separation was close to 34 km s^{-1} .

Here, we will fit the one-dimensional flux power spectrum in the observations and simulation with the following formula:

$$P_F(k) = A_F \frac{\exp(-k^2 v_c^2)}{2\pi} \int_k^\infty dk' k' P_{3D}(k') , \quad (4)$$

where $P_{3D}(k)$ is given by equation (3). We will first obtain fits with the two free parameters A_F and v_c , and then add the slope n in §5.5. Equation (4) applies a Gaussian smoothing directly to the 1D power spectrum, instead of smoothing in three dimensions and then converting to the one-dimensional spectrum (as done in Croft et al. 1999). We will find later (in Fig. 11) that equation (4) agrees well with the low- k [< 0.04 (km s⁻¹)⁻¹] flux power spectrum of the simulation and, most importantly, the best fit for the slope parameter coincides with the real space linear theory slope predicted from the initial perturbations. While the 3D Gaussian smoothing provides a better fit for the power spectrum on very small scales than the 1D Gaussian smoothing, we have found that the best fit parameters with the 3D smoothing do not return the correct value of the spectral index n of the model used in the simulation (the basic reason is that the effect of the 3D smoothing on $P_F(k)$ extends to larger scales than the 1D smoothing). This is not inconsistent with Croft et al. (1998), because we extend the fit to smaller scales.

In Appendix C, we give a justification of the fitting formula in eq. (4) in the limit of large scales, showing that the flux power spectrum must be proportional to the one-dimensional mass power spectrum (see also Scherrer & Weinberg 1998).

Notice that in strict linear theory we should include the effects of peculiar velocities in the transformation from three to one dimensional power, which affect the shape of the power spectrum (Hui 1999; McDonald & Miralda-Escudé 1999a). However, these linear theory results work only on extremely large scales, and in the range of scales we explore here (where the density fluctuations are not much smaller than unity), the higher-order effects are important and opposite to the linear effects. Like Croft et al. (1998), we find that the slope of the simulation power spectrum on large scales is consistent with the *real space* linear theory slope (or equivalently, the peculiar velocity parameter β is quite small).

We first fit equation (4) to the observations and simulations leaving as free parameters the amplitude A and the Gaussian cutoff v_c only. All the other parameters are held fixed at the values they have in the simulation in linear theory (we will let the spectral index n vary later, in §5.5). Table 5 gives the best fit values of these two parameters. For each simulation output (at redshift $z = 2, 3, 4$) we perform three separate fits using the mean flux decrements $\bar{F} = 0.475, 0.684,$ and 0.818 . The result for the amplitude parameter is listed in terms of the contribution to the variance per unit interval of $\ln k$, $\Delta_{3D}^2(k_p) = (2\pi^2)^{-1} k_p^3 P_{3D}(k_p)$ [where $P_{3D}(k)$ is given by eq. (3) with the value of A to fit P_F in eq. (4)]. The value of k_p is $k_p = 0.04$ (km s⁻¹)⁻¹ at $z = 3$, and is held constant in comoving coordinates. The reason for this choice of k_p will be made clear below, in §5.6.

In order to perform the same fits to the flux power spectrum predicted by the simulation,

Table 5. Fitted parameter values for equation (4).

$P_F(k)$ from:	z	\bar{F}	$\Delta_F^2(k_p)$	v_c (km s^{-1})	χ^2/ν	ν
obs.	3.89	0.475	0.0392 ± 0.0024	21.6	1.2	10
obs.	3.00	0.684	0.0370 ± 0.0021	25.4	0.77	10
obs.	2.41	0.818	0.0321 ± 0.0021	28.8	1.4	9
sim.	4	0.475	0.0436 ± 0.0010	21.9	2.2	5
sim.	4	0.684	0.0370 ± 0.0009	20.6	1.9	5
sim.	4	0.818	0.0247 ± 0.0006	19.2	2.6	5
sim.	3	0.475	0.0511 ± 0.0014	23.8	1.4	5
sim.	3	0.684	0.0442 ± 0.0012	23.0	1.3	5
sim.	3	0.818	0.0290 ± 0.0007	21.5	1.6	5
sim.	2	0.475	0.0635 ± 0.0019	29.4	0.36	3
sim.	2	0.684	0.0544 ± 0.0018	28.7	0.26	3
sim.	2	0.818	0.0347 ± 0.0012	26.7	0.11	3

Note. — The fitted power spectrum amplitude is given in terms of $\Delta_F^2(k_p) = (2\pi^2)^{-1}k_p^3 P_{F3D}(k_p)$ where $k_p = 0.04 (\text{km s}^{-1})^{-1}$ at $z = 3$ (and is held constant in comoving coordinates).

we have generated approximate error bars by dividing the lines of sight through the simulation box into twelve groups and measuring the dispersion among them. The groups are defined by the four quadrants of each of the three faces of the simulation cube. We expect that this is an underestimate of the actual errors that would be found if many simulation boxes were available because the twelve groups are not independent, but these error bars should give reasonable best values for fitted parameters.

Even though the power spectrum of the optical depth should have a sharp cutoff at the thermal broadening scale, the transformation to transmitted flux creates small scale power, so the Gaussian cutoff cannot be expected to fit on small scales. We choose the maximum k values to use in the fits (k_{max}) by estimating where equation (4) begins to fit the simulation outputs poorly. We use $k_{max} = 0.04 \text{ (km s}^{-1}\text{)}^{-1}$ for $z_{obs} = 3$ and $z_{obs} = 3.89$, and $k_{max} = 0.032 \text{ (km s}^{-1}\text{)}^{-1}$ for $z_{obs} = 2.41$. The cutoff k_{max} corresponds roughly to v_c^{-1} and decreases with time because v_c increases with time.

The values of χ^2 for the fits all have probabilities higher than 5% with the exception of the fit to the $z = 4$ output of the simulation with $\bar{F} = 0.818$. The probability of χ^2 exceeding its value for the worst fit is $\sim 2\%$, but this is probably acceptable because our simulation error bars are likely to be slightly underestimated.

5.3. Redshift Evolution of the Power Spectrum

If the Ly α forest is in fact governed by gravitational evolution, we know that the amplitude of the fluctuations should generally increase with time. In the linear regime, and when $\Omega(z) \simeq 1$ (a very good approximation in the model we use at $z > 2$), the amplitude should grow proportionally to the scale factor. However, when analyzing the flux power spectrum, its amplitude is affected by the mean flux decrement which is also evolving with redshift.

The observed flux power spectrum at all three redshift bins is plotted as the symbols (pentagons at $z = 4$, squares at $z = 3$ and triangles at $z = 2$) in Figure 7. Error bars are shown at $z = 4$ only to avoid cluttering. The lines are analytic fits to the data points using equation (4). These analytic fits will be used in detail below to measure the amplitude of the power spectrum at each redshift, but here we use them only to qualitatively visualize the redshift evolution. The flux power spectrum increases with redshift, contrary to the expected decrease of the mass power spectrum. The reason is the fast increase in the mean flux decrement with redshift. We can understand the effect of the mean flux decrement by considering the limiting case where all absorbers are optically thin; clearly, for fixed density fluctuations the amplitude of the flux fluctuations should grow proportionally to the flux decrement.

To see that the power spectrum decreases with redshift as expected when the effect of the flux decrement evolution is removed, we plot in Figure 8 the flux power spectrum of the numerical simulation at the redshift outputs $z = 2, 3, 4$, normalizing the optical depth to yield a fixed mean flux decrement $\bar{F} = 0.684$ at all three redshifts. In the limit of large scales, the power is now

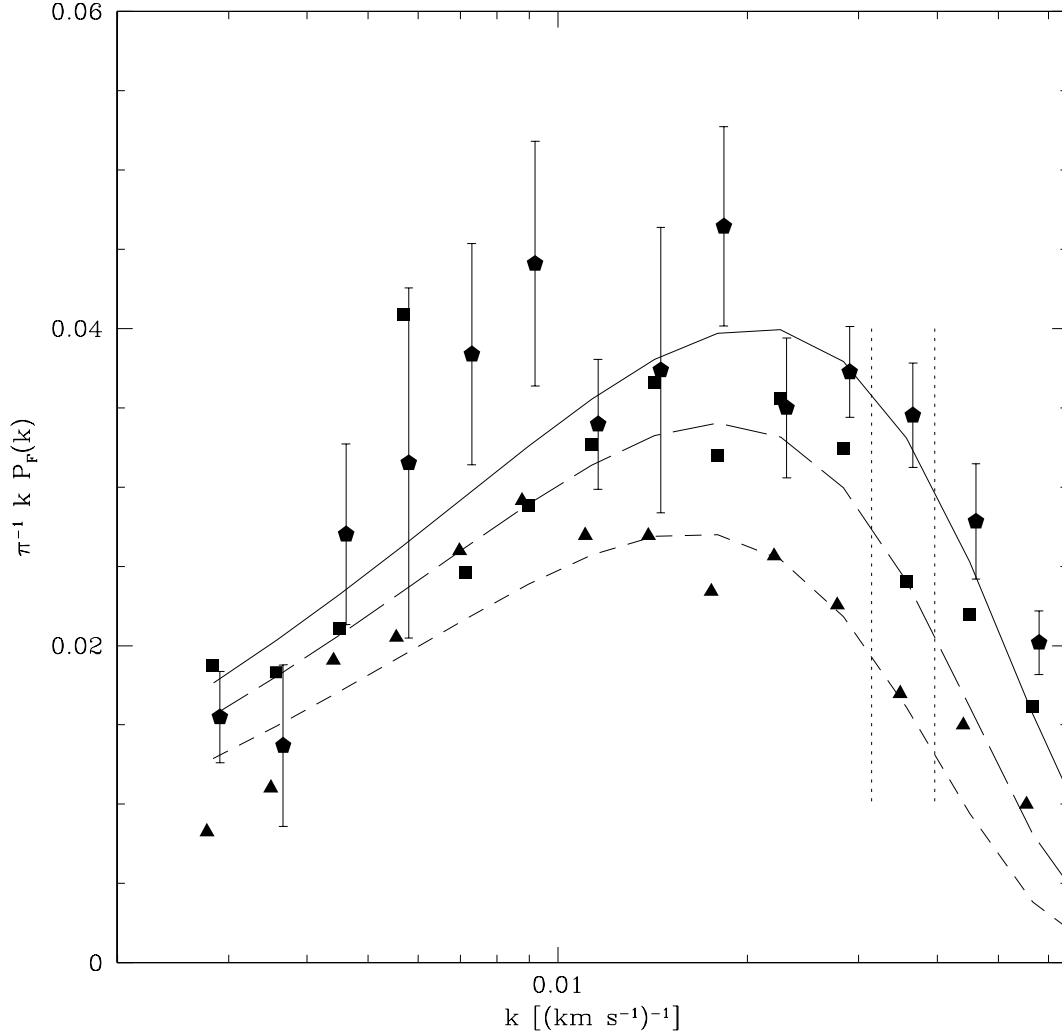


Fig. 7.— The observed one dimensional power spectrum of F along the line of sight for three redshift intervals. The points show the observed $P_F(k)$ values while the lines are analytic fits to the points. The redshifts $\bar{z} = 3.89$, 3.0 , and 2.41 are symbolized by pentagons and the solid line, squares and the dotted line, and triangles and the dashed line, respectively. The power is reduced with decreasing redshift because of the change in the mean flux decrement. The fits are obtained using only points at k smaller than the left vertical dotted line for $\bar{z} = 2.41$, and the right vertical dotted line for $\bar{z} = 3.0$ and $\bar{z} = 3.89$.

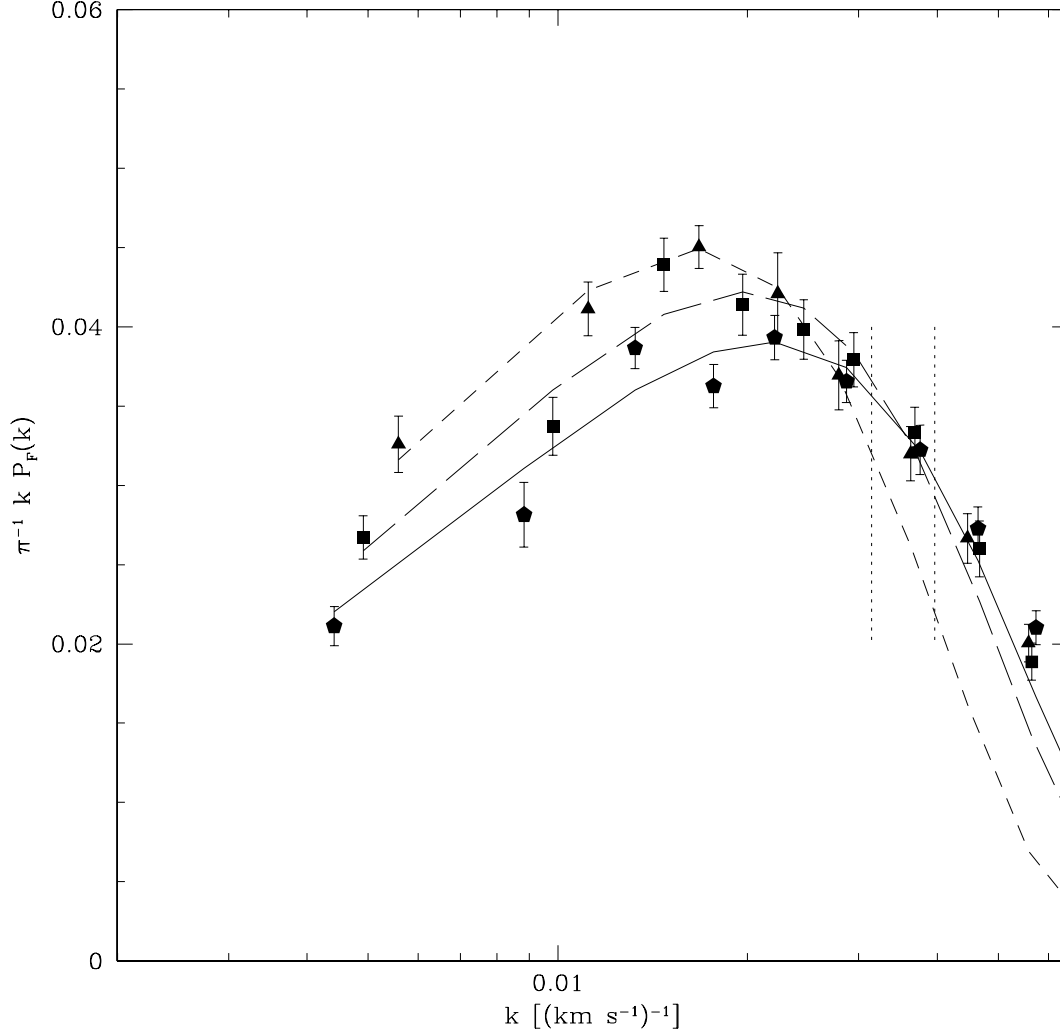


Fig. 8.— The simulated flux power spectrum for the three redshift outputs with optical depths scaled to produce $\bar{F} = 0.684$. The points show the values of $P_F(k)$ at the modes of the periodic simulated box, and the lines are analytic fits to the points. The redshifts $\bar{z} = 4, 3,$ and 2 are symbolized by pentagons and the solid line, squares and the dotted line, and triangles and the dashed line, respectively. We see that the large scale power increases with time as expected when the mean flux decrement is fixed. The fits use only points to the left of the leftmost vertical dotted lines for $z = 2$, and the rightmost vertical dotted line for the other two redshifts. Note that the velocity scale corresponding to a given comoving scale is different for the three redshifts.

increasing as expected. But if the simulated spectra are normalized instead to the observed flux decrements at $\bar{z} = 2.41, 3.00$ and 3.89 , then they have an inverted evolution matching the observed one, as was shown in Figures 5a,b,c.

We notice that the flux power spectrum still decreases more slowly than a^2 in Figure 8. The reason for this is more complex: in the limit of large scales, the flux power spectrum should generally be related to the mass power spectrum by a constant factor (see Appendix C), however this factor depends on the amplitude of fluctuations on the Jeans scale, which changes with time. The factor also depends more weakly on the gas density-temperature relation and other quantities which are changing with redshift.

5.4. The Amplitude of the Observed Power Spectrum Relative to the Simulation

We have already compared qualitatively the observed flux power spectrum observations and the numerical simulation in §5.1. Now we want to use this comparison more quantitatively to determine the amplitude of the primordial density perturbations required to fit the observations. The most straightforward method to implement this fit would be to have several simulations with different amplitudes for the power spectrum. However, since we have only one simulation, we shall instead use the three redshift outputs at $z = 2, 3, 4$ as being equivalent to the results of three different models at the same redshift, having amplitudes of the initial fluctuations in the proportion $3 : 4 : 5$. This assumes a self-similarity in the evolution of the Ly α forest, where reducing the initial amplitude of the power spectrum is equivalent to reducing the scale factor by the same factor. This self-similarity is exact for the dark matter (and assuming $\Omega(z) \simeq 1$). For gas it is broken on small scales by the hydrodynamic effects of the temperature. We will be neglecting here any changes in the relation between the flux and the mass power spectra that are due to a difference in the effects of the gas temperature at different redshifts. Any such changes should probably be highly dependent on the heating mechanisms in the IGM, affected by the model of the ionizing sources and of reionization that is adopted (see Miralda-Escudé & Rees 1994; Hui & Gnedin 1997).

We start by comparing each one of the three simulation outputs at redshifts $z_{sim} = 2, 3, 4$ to each of the three redshift bins in the data, $z_{obs} = 2.41, 3.00, 3.89$. For each one of the nine comparisons, we go through the following steps in order to compute a χ^2 statistic measuring the degree to which the simulation is consistent with the observations:

1. We set the mean transmitted flux \bar{F} in the simulation to match the \bar{F} of the observation, by rescaling the optical depth. This is an important step because, as we have seen in §5.3, the amplitude of the flux power spectrum is highly sensitive to \bar{F} .

2. We fit the parameters $\Delta_{\bar{F}}^2(k_p)$ and v_c (defined in §5.2) to the simulated power spectrum using equation (4), keeping n and Γ fixed to the values of the initial power spectrum assumed in the simulation.

3. We obtain the dimensionless quantity $k P_F(k)$ from the fit to the simulated power spectrum at redshift z_{sim} (expressing k in units of the Hubble velocity), and transform it to redshift z_{obs} by rescaling k by the factor $[H(z_{sim})/H(z_{obs})][(1+z_{obs})/(1+z_{sim})]$, in order to compare the power spectra of the observations and simulations at the same comoving scale.

4. We compute the χ^2 statistic from the difference between the observed power spectrum and the fit to the simulation at every k bin of the observational data, up to $k_{max} = 0.032 \text{ km s}^{-1}$ for all redshift bins, using the error bars of the observations.

In Figure 9 we compare the fits to the power spectra from all three simulation outputs to the observed $P_F(k)$ in all three redshift bins. The values of χ^2/ν for all of these comparisons (where ν is the number of degrees of freedom) are listed in Table 6. It is clear from Figure 9 that the amplitude of the power spectrum needs to be decreased in order to match the observations at large scales. From Table 6, we can see, for example, that the observations at $z_{obs} = 3$ are consistent with the simulation at $z_{sim} = 4$, but inconsistent at $z_{sim} = 3$; this yields an upper bound of $\sigma_8 < 0.79$ for the power spectrum normalization of the Λ CDM model of the simulation, since the amplitude has to be lower than that used in the simulation. At the same time, the observation at $z_{obs} = 2.41$ is significantly better fit by the simulation output at $z_{sim} = 3$ than the one at $z_{sim} = 4$; to within the significance level implied by the difference in the χ^2 in Table 6, this implies a lower limit $\sigma_8 > 0.54$.

Because the amplitudes of the simulation outputs appear to bracket the observations, the obvious next step is to interpolate between the simulation outputs to obtain a best fit value for the power spectrum amplitude. For this purpose, we fit the power-law $\Delta_F^2(k_p) = C a_{sim}^\alpha$ to the three values of the amplitude $\Delta_F^2(k_p)$ at $z_{sim} = 2, 3, 4$ (where $a_{sim} \equiv (1+z_{sim})^{-1}$) listed in Table 5, which were obtained by fitting equation (4) to the simulated power spectrum in §5.2. We do this for all three values of the mean transmitted flux at the three redshift bins of the data. The results are given in Table 7.

To find the best fit for the power spectrum amplitude, we now fit the observational data at each redshift bin with the two parameters $\Delta_F^2(k_p)$ and v_c , but expressing the amplitude of the flux power spectrum in terms of a_{obs}/a_{sim} , where a_{sim} is determined from the power-law fit $\Delta_F^2(k_p) = C a_{sim}^\alpha$ with the parameters in Table 7. Figure 10 shows the value of $\Delta\chi^2$ as a function of a_{obs}/a_{sim} , when we let v_c vary, for each redshift bin z_{obs} ($\Delta\chi^2$ is equal to the χ^2 function minus its minimum value). The solid thick line is the sum of all three χ^2 functions (subtracting the minimum value), thereby yielding the value and error of the amplitude when it is required to be the same at all three redshift bins. The result is $a_{obs}/a_{sim} = 0.856 \pm 0.042$; this is equal to the factor by which we need to multiply the initial mass fluctuations in the simulation to obtain the best match to the observations. The error bar is increased to $a_{obs}/a_{sim} = 0.856 \pm 0.052$ when including the error in the determination of the power spectrum amplitude from the simulation (see Table 5, we use the error on the $z = 3$, $\bar{F} = 0.684$ amplitude), determined as explained in §5.2. The χ^2 value of the power spectrum fit of all three redshift bins combined, $\chi^2 = 35$ with 31 degrees of freedom (35 data points minus four free parameters), should be exceeded randomly 28% of the time. This implies

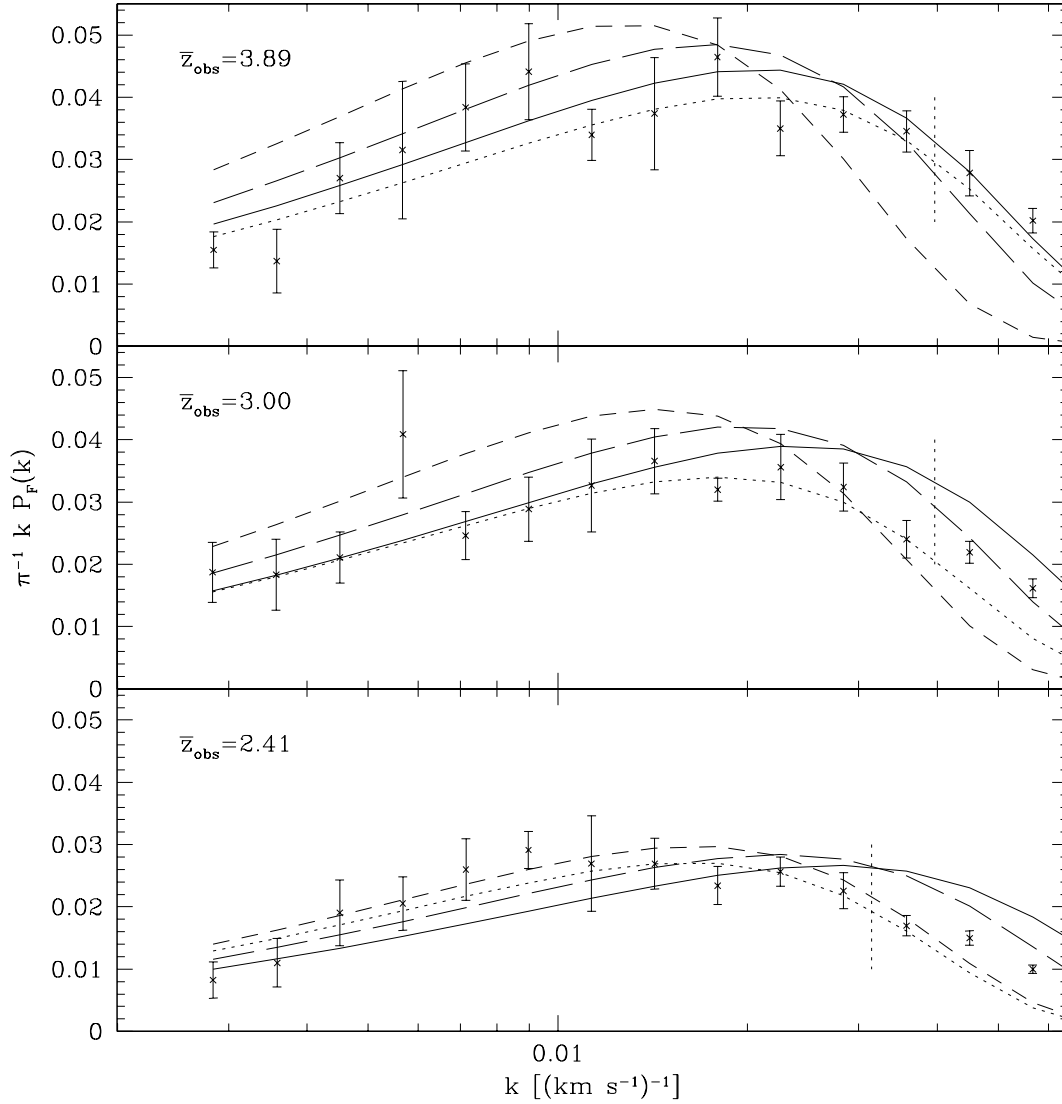


Fig. 9.— The observed power spectrum compared to the fitted simulation outputs for $z = (4, 3, 2)$ represented by (*solid, long-dashed, dashed*) lines. The simulated power spectra are computed after \bar{F} has been fixed to match the observation that they are being compared to. The dotted line is a fit to the observational data.

Table 6. Values of χ^2/ν for direct comparisons between the observational data points and fits to power spectrum in the simulation.

z_{obs}	$z_{sim} = 4$	$z_{sim} = 3$	$z_{sim} = 2$
3.89	1.8	3.6	7.6
3.00	1.7	4.1	7.2
2.41	2.3	1.8	1.6

Note. — Each comparison uses only points with $k < 0.032 \text{ (km s}^{-1}\text{)}^{-1}$ and has $\nu = 11$.

Table 7. Parameters for interpolation between the power spectrum amplitudes at different redshifts in the simulation.

\bar{F}	$C(\bar{F})$	$\alpha(\bar{F})$
0.475	0.0513	0.735
0.684	0.0440	0.74
0.818	0.0288	0.670

Note. — The interpolation formula is $\Delta_F^2(k_p) = C(\bar{F})(a_{sim}/0.25)^{\alpha(\bar{F})}$.

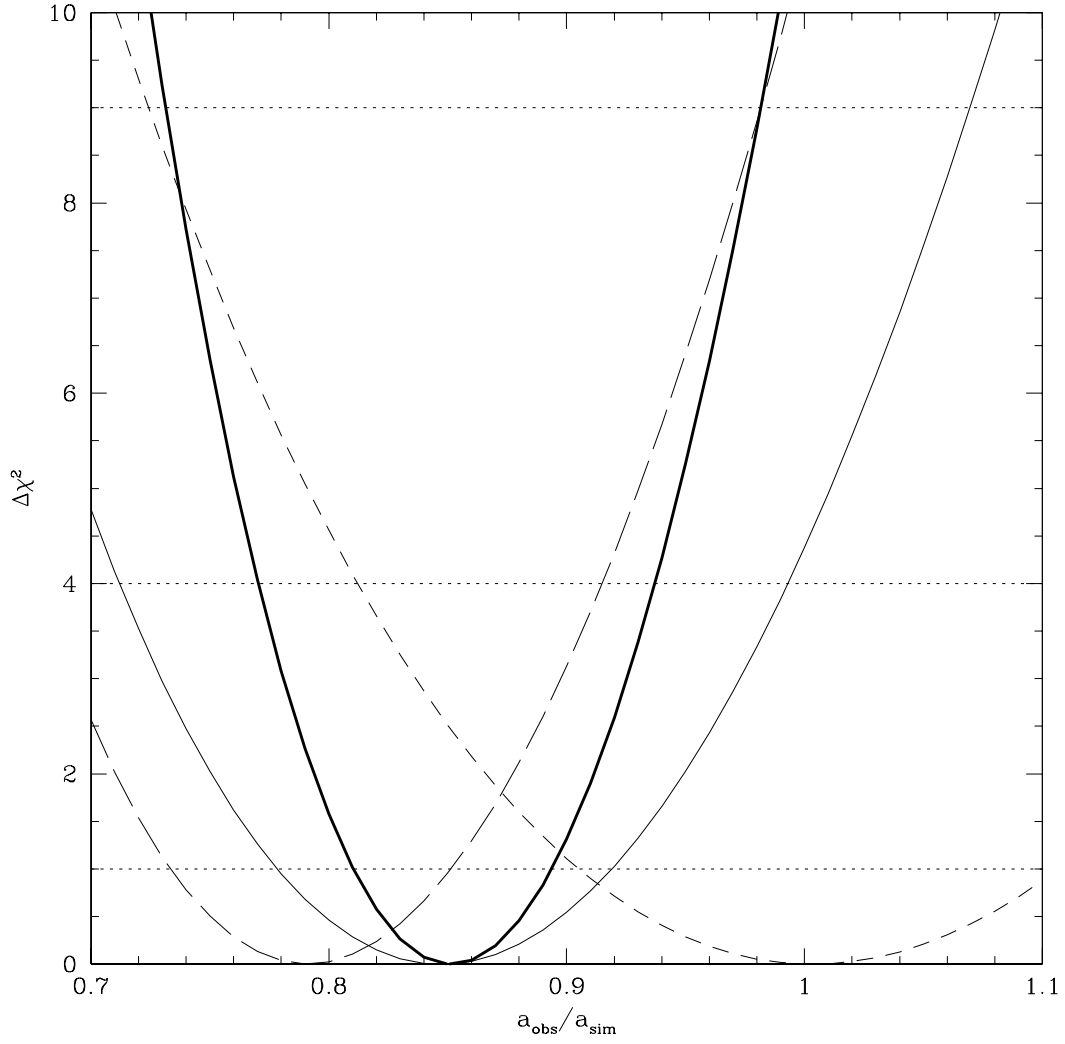


Fig. 10.— Fits comparing the interpolated amplitude in the simulation to the amplitude of the observations. The thin lines show $\Delta\chi^2$ for $z_{\text{obs}} = (3.89, 3.00, 2.41)$ (*solid, long-dashed, short-dashed*). The thick line shows the combination of all three redshifts.

that our observational data are perfectly consistent with the redshift evolution of the flux power spectrum predicted by the simulation, and with the shape in equation (4) when v_c is allowed to vary.

To conclude, our result is that the rms amplitude of the initial fluctuations of the Λ CDM model in the simulation we use should be reduced by the factor 0.856 ± 0.052 , or to $\sigma_8 = 0.68 \pm 0.04$. A possible modeling error in the determination of this amplitude is that the flux power spectrum is also affected by the temperature distribution of the gas, and we are relying on the temperatures given by the simulation for our measurement of the amplitude. For example, if a temperature-density relation $T \propto \rho^{\gamma-1}$ is followed, the neutral density varies with density as $n \propto \rho^{2-0.7(\gamma-1)}$ in photoionization equilibrium, so the relation between the flux and mass power spectra depends on $\gamma - 1$.

We have assumed in our analysis that the error bars on the measured power spectrum points are uncorrelated. We have verified this by re-running the amplitude fitting procedure described above on 100 bootstrap realizations of the observed power spectrum for each redshift bin. We measure the dispersion in the best fit values of a_{obs}/a_{sim} and find $(\pm 0.054, \pm 0.076, \pm 0.168)$ for $z = (4, 3, 2)$. The errors estimated using $\Delta\chi^2 = 1$ in Figure 10 are $(\pm 0.07, \pm 0.06, \pm 0.11)$. The errors at lower redshift are probably becoming more correlated, as expected given the increased non-linearity, but the effect is still not large. We compute a weighted mean and error for a_{obs}/a_{sim} using these error bars and find $a_{obs}/a_{sim} = 0.845 \pm 0.043$ while we found $a_{obs}/a_{sim} = 0.856 \pm 0.042$ above. The difference is clearly not important for our current level of precision, but it may become important when a larger sample of quasars is available.

5.5. The Slope of the Power Spectrum

We now show that the slope parameter n of the power spectrum we measure from both the simulation and the observations (by fitting equation [4]) is consistent with the linear theory, real space power spectrum used to set the initial conditions of the simulation.

We start analyzing the spectra of the numerical simulation. In Figure 11, the $\Delta\chi^2$ value is plotted as a function of n , where A_F and v_c are free parameters at each redshift. The parameter $\Gamma(z)$ in the power spectrum formula is still fixed to the model assumed in the simulation. The result is consistent with $n = 0.95$ at all three redshift bins. The best fit is $n = 0.93 \pm 0.07$. We use the error bar given by $\Delta\chi^2 = 1$ for the $z = 3$ output only because the three curves are largely evolved versions of each other, so the values of n obtained from different simulation outputs are not independent. It is especially reassuring to see that the widely different mean flux decrements at the different redshifts do not seem to have any systematic effect on the slope.

In Figure 12 we present the same $\Delta\chi^2$ functions for the observations. We again allow A_F and v_c to vary independently at each redshift (six free parameters) but fix $\Gamma(z)$ to the value given by the simulation parameters. We find an overall best fit value of $n = 0.96 \pm 0.08$ with $\chi^2/\nu = 1.13$

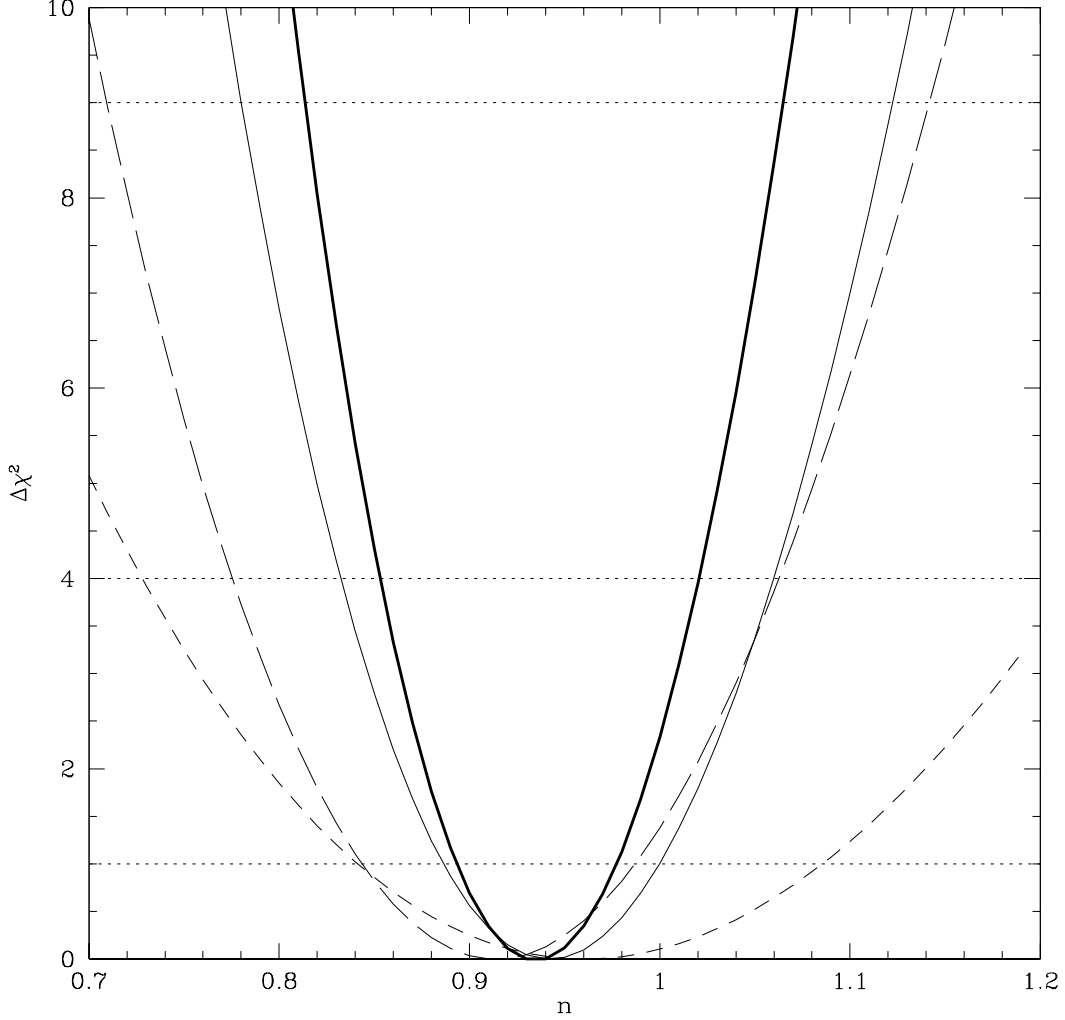


Fig. 11.— Fits to the power spectrum in the simulation with varying n . The linear theory value of n in the initial conditions was $n = 0.95$. The thin lines are $\Delta\chi^2 = \chi^2 - \chi_{min}^2$ for $z = (4, 3, 2)$ (*solid, long-dashed, short-dashed lines*). The thick solid line is the sum of the three redshifts. At each redshift the mean flux decrement was fixed to the value of the nearest observational redshift bin. For each redshift the amplitude and a 1D cutoff were fitted independently. Note that the statistical error on the combined result is larger than $\Delta\chi^2$ indicates because the three sets of errors are not independent. The best fit value is $n = 0.93 \pm 0.07$ where the error ± 0.07 is the error for the $z = 3$ output alone, *not* the sum of the three. The best fits have $\chi^2/\nu = (2.7, 1.6, 0.16)$ for $z = (4, 3, 2)$ and $\nu = (4, 4, 2)$. The probability for the $z = 4$ value of χ^2 is only 3% but this is probably reasonable because we expect that the error bars on the simulation are somewhat underestimated (see text).

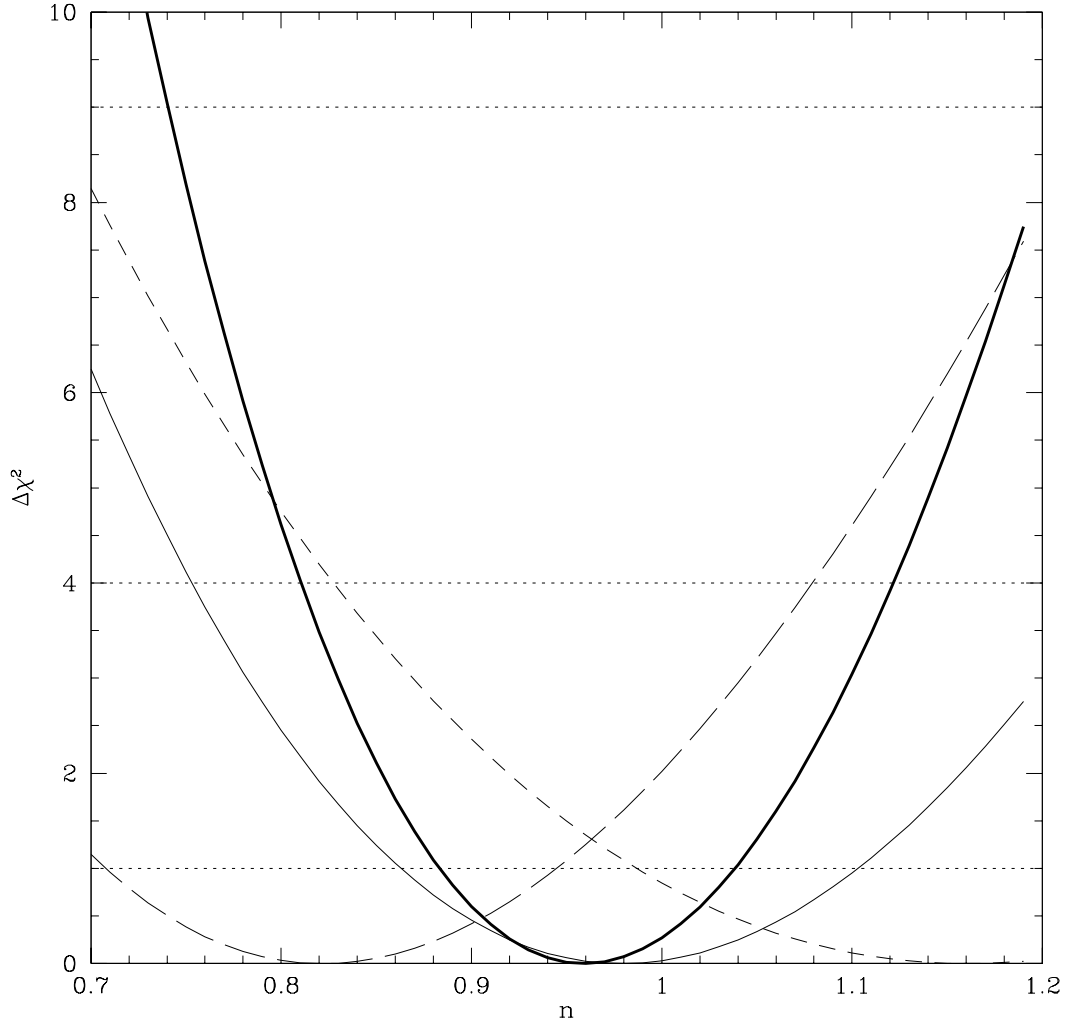


Fig. 12.— Fits to the power spectrum of the observations with varying n . The thin lines are $\Delta\chi^2 = \chi^2 - \chi_{min}^2$ for $z = (3.81, 3.0, 2.41)$ (*solid, long-dashed, short-dashed lines*). The thick solid line is the sum of the three redshifts. For each redshift the amplitude and a 1D cutoff were fitted independently. The best fit value overall is $n = 0.96 \pm 0.08$ with $\chi^2/\nu = 1.13$ for $\nu = 28$. The simulation measurement should be used as a correction to give a final result $n = 0.98 \pm 0.11$.

for $\nu = 28$ degrees of freedom.

Since our test of the slope fitting procedure using the simulation (Figure 11) yielded $n = 0.93 \pm 0.07$, when the true linear theory slope of the model was $n = 0.95$, we shall assume that the same offset $\Delta n = -0.02 \pm 0.07$ should be present in the observations. We use this offset as a correction to the observational slope and add the error in quadrature. The final result for the estimated linear theory slope is then $n = 0.98 \pm 0.11$. Note that this result assumes that the deviation from a power-law for the power spectrum of the real universe matches the deviation in the Λ CDM model of our simulation.

5.6. Joint Fit for the Amplitude and Slope

The result for the slope in §5.5 was obtained independently in the three redshift bins, without requiring the amplitudes to follow the evolutionary law of Table 7. In fact, generally it would not be valid to use the values of $C(\bar{F})$ and $\alpha(\bar{F})$ in this Table when the initial power spectrum does not have the same slope as in the simulation. However, the result we found for the slope is very close to that of the simulation. This justifies a joint fit for the amplitude and slope using the interpolation constants in Table 7.

The joint fit applied to the simulation yields $a_{obs}/a_{sim} = 1$, by definition, and $n = 0.94 \pm 0.04$. This result is close to that found in §5.5, with a smaller error bar mostly because this is now a combined fit to all three redshifts. For the same fit to the observations, the amplitude is $a_{obs}/a_{sim} = 0.85 \pm 0.04$ and the slope is $n = 0.92 \pm 0.07$. The reduction by two in the number of free parameters (since the amplitudes at the three redshifts are now tied by the formula from Table 7) is accompanied by an increase of 3.3 in χ^2 for the best fit to the observations. Including the correction and error from the fit to the slope in the simulation ($\Delta n = -0.01 \pm 0.07$ using the error bar from only one redshift output) gives a final result $n = 0.93 \pm 0.10$.

The value of k we use to specify the amplitude, $k_p = 0.04 \text{ (km s}^{-1}\text{)}^{-1}$ at $z = 3$, was chosen to make the error bars on the slope and amplitude independent for this measurement. Note that this pivot k is five times larger than the pivot used by Croft et al. (1999) because we have used data on smaller scales and also weighted the fits using the statistical error bars instead of the more conservative weighting (that favored large scales) used by Croft et al. (1999). The fact that we use the 1D power spectrum for fitting also contributes to the large value of our k_p , because a data point $P_{1D}(k)$ is an integral over the 3D power at wave numbers larger than k . We are able to take advantage of our higher resolution data because we also have a higher resolution simulation to test the procedure. However, these errors are statistical only, and do not include systematic errors due to the way we model the flux power spectrum as a function of the mass power spectrum based on the simulation used here.

Our result is that the observational data appears to favor a value of $\sqrt{P(k_p)}$ at $k_p = 0.04 \text{ (km s}^{-1}\text{)}^{-1}$ that is 0.85 ± 0.05 times the amplitude of the simulation (after adding the error in the deter-

mination of the simulation amplitude). Computing the value of the linear theory power in the simulation at $k_p = 0.04 \text{ (km s}^{-1}\text{)}^{-1}$ and $z = 3$ we find that our result corresponds to $P_{3D}[k = 0.04 \text{ (km s}^{-1}\text{)}^{-1}, z = 3] = (2.2 \pm 0.3) \times 10^5 \text{ (km s}^{-1}\text{)}^3$ or equivalently $\Delta_\rho^2[k = 0.04 \text{ (km s}^{-1}\text{)}^{-1}, z = 3] = 0.72 \pm 0.09$ where $\Delta_\rho^2(k)$ is the contribution to the mass density variance per unit interval in $\ln k$. Croft et al. (1999) measured $\Delta_\rho^2[k = 0.008 \text{ (km s}^{-1}\text{)}^{-1}, z = 2.5] = 0.57_{-0.18}^{+0.26}$. Using our amplitude measurement at k_p and our measurement of the slope relative to the simulation we find $\Delta_\rho^2[k = 0.008 \text{ (km s}^{-1}\text{)}^{-1}, z = 2.5] = 0.32 \pm 0.07$. The two results are consistent, differing by $\sim 1.3 \sigma$. Note that the change in slope in the CDM power spectrum, between the two pivot points, is important for this comparison.

We have discussed the slope of the power spectrum in terms of the large scale asymptotic slope n because it is simple to relate this number to the simulation initial conditions and cosmology in general. Of course we are really measuring an effective value of the slope on the scale of the Ly α forest. We define the slope parameter n_p to be the slope at $k_p = 0.04 \text{ (km s}^{-1}\text{)}^{-1}$ at $z = 3$. Using equation (3), it is straightforward to compute n_p for a given n . For the value of $\Gamma(z)$ used in the fits, and with $n = 0.95$, we find $n_p = -2.53$. The observational result, $n = 0.93 \pm 0.10$ (or $n = 0.98 \pm 0.11$ using the more conservative method in §5.5), corresponds to $n_p = -2.55 \pm 0.10$ (or $n_p = -2.50 \pm 0.11$). For the pivot point that Croft et al. (1999) used, $z = 2.5$ and $k = 0.008 \text{ (km s}^{-1}\text{)}^{-1}$, the slope of our fitting function is -2.22 for $n = 0.95$ so our result corresponds to -2.24 (-2.19) while they found -2.25 . For measuring the slope at k_p , using the CDM power spectrum shape is not crucially important; however, the extrapolation we use to compare to the Croft et al. (1999) result is only valid if the CDM power spectrum correctly describes the shape of the power spectrum in the real universe.

5.7. The $\Delta_F^2 - \Delta_{mass}^2$ Relation and Possible Modeling Errors in our Result

The ratio of the flux fluctuation amplitude (from Table 5) to the linearly extrapolated mass fluctuation amplitude, $B \equiv [\Delta_F^2 / \Delta_{mass}^2]^{1/2}$, is given in Table 8. This ratio can be thought of as the “bias” of the Ly α forest. However, this factor is not the bias to be applied in linear theory peculiar

Table 8. Ratio of flux fluctuations to linearly extrapolated mass fluctuations in simulation,

$$B = [\Delta_F^2(k_p) / \Delta_{mass}^2(k_p)]^{1/2}.$$

z_{sim}	$B(\bar{F} = 0.475)$	$B(\bar{F} = 0.684)$	$B(\bar{F} = 0.818)$
4	0.264	0.243	0.198
3	0.228	0.212	0.172
2	0.191	0.177	0.142

velocity calculations, because in the Ly α forest a non-linear mapping is applied to the *redshift space* optical depth field to obtain the flux.

The results in Table 8 should allow for an easy comparison with other numerical simulations of the quantity we need to obtain the mass power spectrum amplitude from observations. One of the main uncertainties in the B factor arises from the temperature-density relation, which affects the relation between neutral density and baryon density: $n_{HI} \propto \alpha(T) \Delta_b^2 \propto \Delta_b^{2-0.7(\gamma-1)}$, where Δ_b is the baryon density divided by its mean value, and we have assumed $T \propto \Delta_b^{\gamma-1}$. Increasing γ decreases the optical depth fluctuations for fixed baryon density fluctuations. The theoretical expectation is $0.0 < \gamma - 1 < 0.6$ (Hui & Gnedin 1997), and our simulation falls roughly in the center of this range, giving a potential error of $\sim 10\%$ in $2 - 0.7(\gamma - 1)$. A change in thermal broadening also changes the amplitude of flux fluctuations in a more complicated way by changing the weighting of different densities in the spectra.

6. THE CORRELATION FUNCTION

We now discuss the correlation function $\xi(\Delta v) = \langle \delta F(v) \delta F(v + \Delta v) \rangle$. It is straightforward to measure ξ by directly averaging over the pixels in the spectra. The results are shown in Table 9. It is important to recognize that the error bars we give here are *strongly* correlated and we include them only to give a qualitative idea how large they are. Any statistical comparisons with data should use the full error covariance matrix, which is available in the website given earlier. In Figures 13(a,b,c) we show the correlation function measured from the observations and the simulation. The observation and simulation do not agree well in spite of the good agreement between the power spectra shown in Figure 5. The reason, as we will show below, is that the correlation function computed from the simulation is strongly affected by the finite box size. Figure 14 shows ξ plotted for each of the observed redshift bins. For this figure each correlation function has been divided by the variance, σ_F^2 , at the same redshift, so the curves are all normalized to $\xi(0) = 1$. There is no clear difference between the correlation lengths at the three redshifts.

Finally we show the effect of the box size on the correlation function from the simulation in Figure 15. We first fit to the *power spectrum* of the simulation at $z = 3$ using the linear theory function with a 3D cutoff instead of our usual 1D cutoff. We use the 3D cutoff because this function fits the full range of k , including the small scales. When we Fourier transform the analytic power spectrum using the parameters that fit the simulation, the correlation function obtained is quite different from the one measured directly from the simulation. In fact, the agreement in Figure 13 between the observed and simulated $\xi(\Delta v)$ as $\Delta v \rightarrow 0$ is only a coincidence: the observed correlation function is in fact smaller than in the simulation model, but the correlation function in the simulation is lowered by the finite box size effects to a value close to the observed one. Figure 13 also shows that we can approximately recover the correlation function that is measured from the simulation by summing over the analytic power spectrum using only k values of discrete modes that are actually included in the simulation box.

Table 9. The observed flux correlation function.

$\Delta v_{bin,min}$ (km s^{-1})	Δv_{mean} (km s^{-1})	$\xi(\Delta v, z = 3.89)$	$\xi(\Delta v, z = 3.0)$	$\xi(\Delta v, z = 2.41)$
7	10.5	0.1230 ± 0.0031	0.1132 ± 0.0055	0.0767 ± 0.0069
14	17.5	0.1142 ± 0.0032	0.1071 ± 0.0055	0.0721 ± 0.0067
21	24.5	0.1039 ± 0.0035	0.0993 ± 0.0055	0.0667 ± 0.0065
28	31.5	0.0936 ± 0.0038	0.0911 ± 0.0055	0.0609 ± 0.0062
35	39.53	0.0827 ± 0.0040	0.0820 ± 0.0056	0.0544 ± 0.0059
44.06	49.76	0.0710 ± 0.0043	0.0717 ± 0.0057	0.0469 ± 0.0056
55.47	62.65	0.0595 ± 0.0046	0.0613 ± 0.0059	0.0390 ± 0.0051
69.83	78.87	0.0484 ± 0.0048	0.0514 ± 0.0061	0.0313 ± 0.0047
87.92	99.29	0.0380 ± 0.0049	0.0420 ± 0.0062	0.0240 ± 0.0041
110.7	125	0.0294 ± 0.0048	0.0336 ± 0.0062	0.0178 ± 0.0035
139.3	157.4	0.0211 ± 0.0047	0.0275 ± 0.0056	0.0120 ± 0.0031
175.4	198.1	0.0143 ± 0.0047	0.0227 ± 0.0048	0.0069 ± 0.0026
220.8	249.4	0.0095 ± 0.0049	0.0177 ± 0.0045	0.0037 ± 0.0025
278	314	0.0064 ± 0.0046	0.0104 ± 0.0041	0.0004 ± 0.0023
350	395.3	0.0047 ± 0.0048	0.0078 ± 0.0037	-0.0023 ± 0.0020
440.6	497.6	-0.0010 ± 0.0055	0.0072 ± 0.0035	-0.0003 ± 0.0024
554.7	626.4	0.0027 ± 0.0058	0.0029 ± 0.0035	0.0014 ± 0.0028
698.3	788.5	0.0060 ± 0.0054	0.0033 ± 0.0035	0.0025 ± 0.0017
879.2	992.7	0.0059 ± 0.0038	0.0060 ± 0.0032	0.0005 ± 0.0017
1107	1250	-0.0007 ± 0.0040	0.0051 ± 0.0045	0.0008 ± 0.0017
1393	1573	-0.0014 ± 0.0043	-0.0060 ± 0.0041	-0.0005 ± 0.0019
1754	1980	-0.0042 ± 0.0033	-0.0005 ± 0.0039	-0.0019 ± 0.0016
2208	2493	0.0013 ± 0.0033	-0.0028 ± 0.0032	0.0002 ± 0.0018

Note. — Averaged over bins defined by the velocity separation Δv_{min} , with mean velocity separation Δv_{mean} (the maximum velocity separation for the final bin is $\Delta v_{max} = 2780 \text{ km s}^{-1}$).

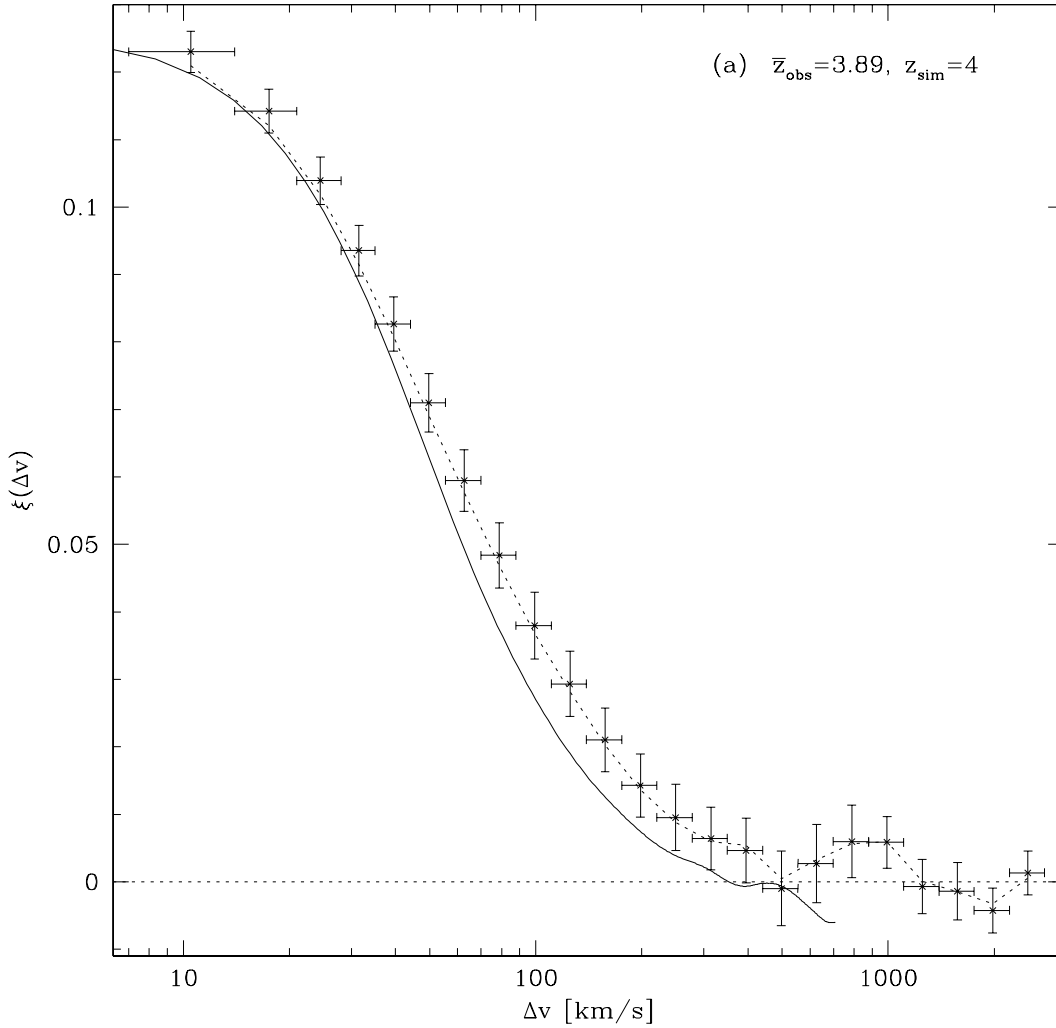
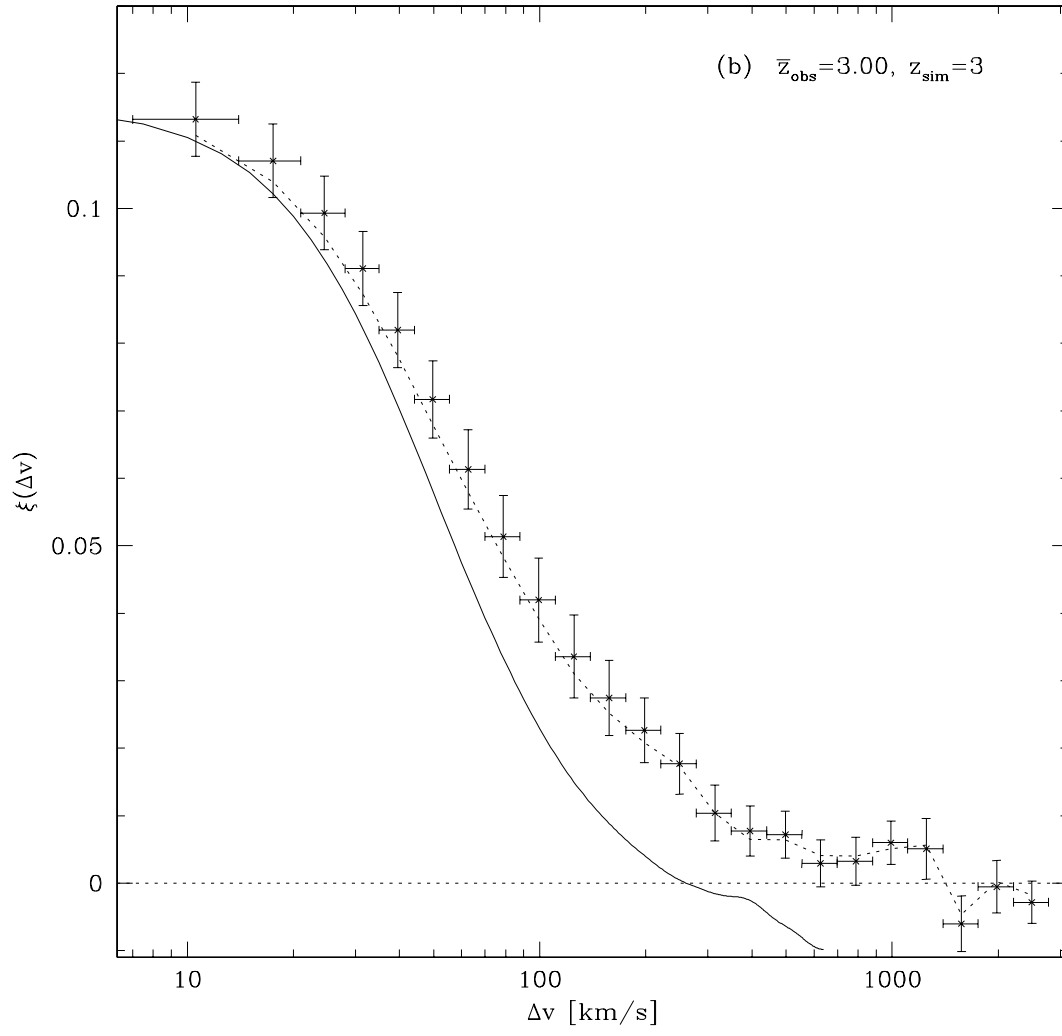
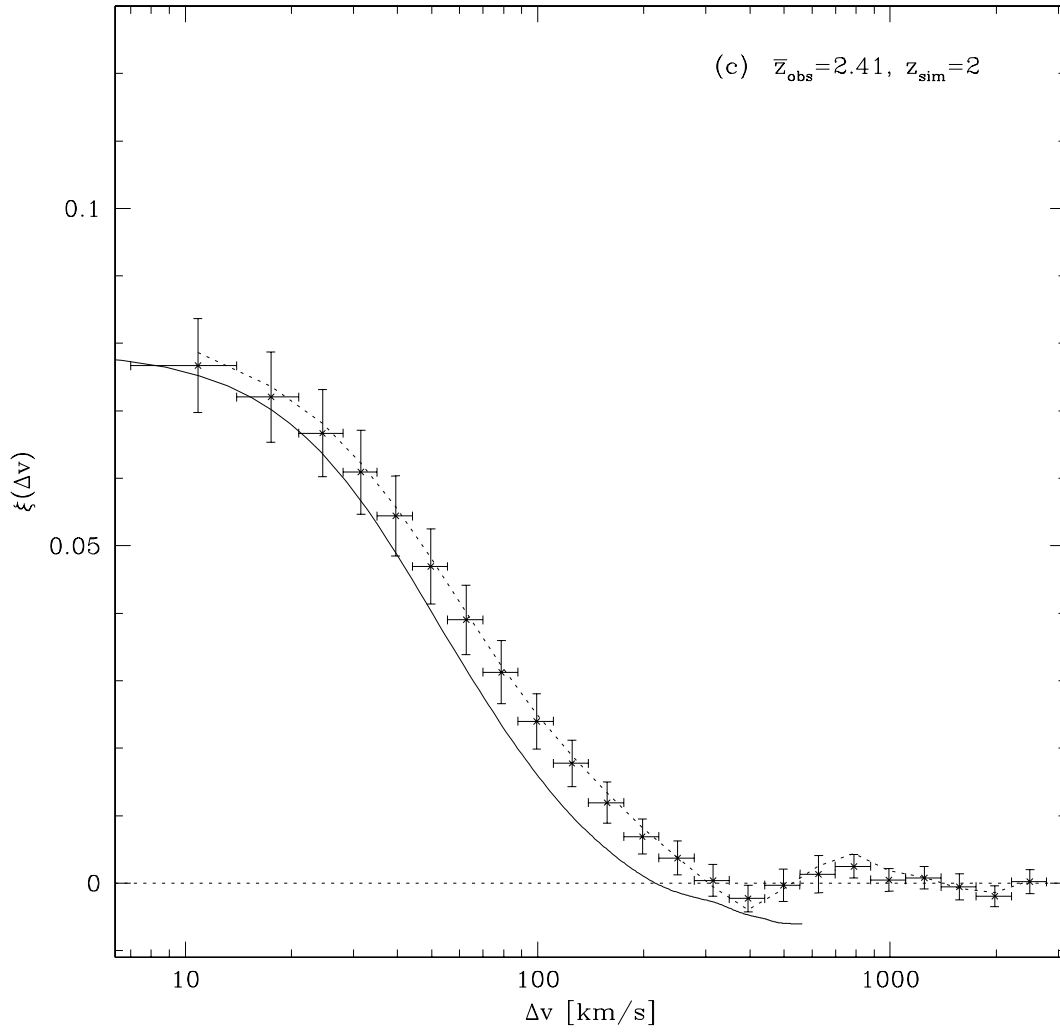


Fig. 13.— The observed correlation function of F as a function of velocity separation along the line of sight (*points with error bars*). The definition of the correlation function is: $\xi(\Delta v) = \langle \delta F(v) \delta F(v + \Delta v) \rangle$ where $\delta F = F - \bar{F}$. The error bars on Δv show the bins used to average the correlation function. The error bars on ξ are too highly correlated to use for statistical analysis without accounting for off-diagonal terms in the error covariance matrix. The dotted line shows the correlation function when the possible metal line regions are included in the computation. The solid line shows the correlation function from the simulation, which is strongly influenced by the finite box size. (a) shows $\bar{z} = 3.89$, (b) shows $\bar{z} = 3.00$, and (c) shows $\bar{z} = 2.41$.





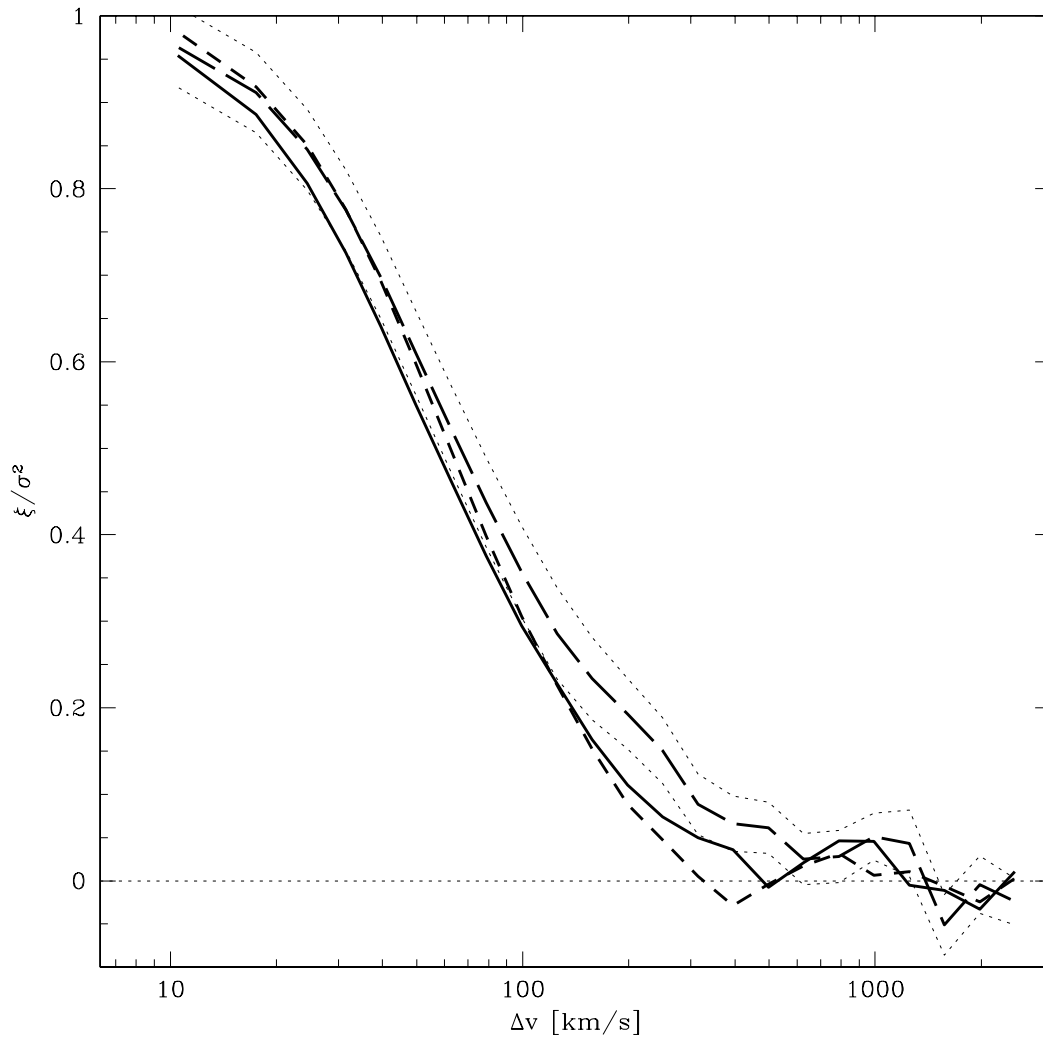


Fig. 14.— Comparison of the correlation functions for $z = 3.89$ (*solid line*), $z = 3.0$ (*long-dashed line*), and $z = 2.41$ (*short-dashed line*). The amplitude of each curve has been divided by $\sigma_F^2(z)$ so that $\xi(0) = 1.0$ for each. The thin dotted lines connect the error bars on the $z = 3$ correlation function.

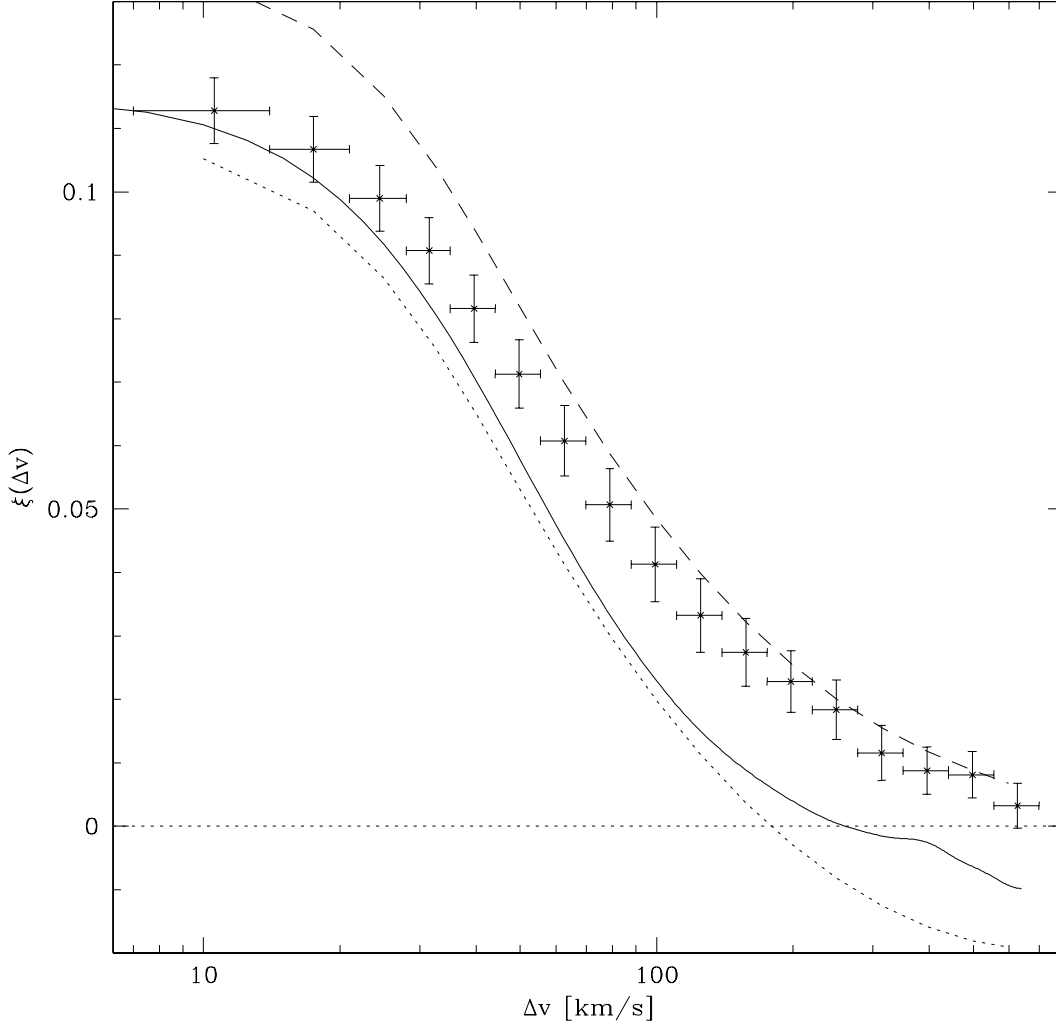


Fig. 15.— The effect of the finite box size of the simulation. The points with error bars show the observed ξ for reference. The solid line shows ξ measured from the simulation. The dashed line shows ξ computed by integrating an analytic power spectrum with parameters determined by a fit to the power spectrum measured from the simulation. The fit uses a Gaussian cutoff on the linear theory 3D power spectrum and fits the entire range of k fairly well. The dotted line shows the correlation function calculated from the same analytic power spectrum, but here it is computed by summing over the 1D modes actually in the box instead of integrating over all k . There is a discrepancy between the solid and dotted lines because the mean along each line of sight through the simulation can vary from the overall mean and the dotted curve is computed from a fit to the simulation power spectrum rather than the power spectrum itself.

7. DISCUSSION

We have presented an observational determination of the PDF, the power spectrum, and the correlation function of the transmitted flux in the Ly α forest, using a sample of eight quasars over the redshift range $2.1 < z < 4.4$. All our results are given with error bars that include the variance of our sample of eight quasars. These results can be compared to the predictions of any cosmological simulations of a given theory, after instrumental resolution and noise with the same amplitude as in our data are added to the simulated spectra. Any future observational determinations of the same quantities from other data sets will also be easily comparable.

In our opinion, there are two main objectives in the accurate measurement of the statistics of the one-dimensional random field of the transmitted flux in the Ly α forest. The first is to test the idea that the Ly α forest is entirely explained by an IGM that is photoionized and heated by the known sources of ionizing radiation (AGNs and galaxies), which evolves gravitationally as described by a large-scale structure theory based on the presence of cold dark matter and adiabatic, Gaussian primordial fluctuations. The second objective is to measure some of the parameters of the large-scale structure model from the Ly α forest observations.

Even though there are a large number of parameters required to fully describe the cosmological and large-scale structure model, and the population of sources of ionizing radiation, only certain combinations of these parameters are important to determine the observable properties of the Ly α forest to a first approximation. A simple intuitive understanding of what these parameters are can be developed by considering a simplified model where the power spectrum of fluctuations is approximated as a power-law, and the IGM follows a simple density-temperature relation $T = T_0 (\rho/\bar{\rho})^{\gamma-1}$. In this case, the temperature T_0 determines a Jeans scale, and all the statistical properties of the Ly α optical depth should depend only on the amplitude of the density fluctuations at the Jeans scale, σ_J , the effective power-law index near the Jeans scale n_J , and γ (it is understood here that all these parameters depend on redshift for any given model). In addition, varying the temperature T_0 (while keeping σ_J , n_J and γ fixed) should cause a rescaling of all the statistical properties of the Ly α forest in velocity (proportional to the Jeans scale, or $T_0^{1/2}$), and varying the parameter μ (defined in eq. 1) should cause a rescaling of the optical depth. Therefore, in this simplified model the Ly α forest depends on five parameters only, and the changes under two of them are trivially obtained by rescalings. Only σ_J and n_J contain information on the large-scale structure model; T_0 and γ depend on how the IGM was reionized (e.g., Miralda-Escudé & Rees 1994; Hui & Gnedin 1997) as well as the power spectrum (through the effects of shock-heating), and μ depends on Ω_b , $H(z)$, and the intensity of the ionizing background.

More exact predictions for the Ly α forest obtained in hydrodynamic simulations will depend on more parameters, due to effects that are neglected in the simplified model just discussed. The true distribution of density and temperature of the gas has of course a scatter around a mean relationship; this mean relationship also deviates from a power-law. This distribution depends on the ratio of the cooling rate to the Hubble rate, which is proportional to the new parameter

$\Omega_b h^2 / H(z)$. In addition, the effects of cooling imply that changing T_0 will no longer result in a simple rescaling in velocity of all statistical properties of the Ly α forest, since the cooling rate has a complex dependence on temperature that breaks the self-similar scaling. These effects should be important only at high densities, where cooling is important; at low densities, the thermal evolution of the IGM naturally produces the “Hui-Gnedin relation” (Hui & Gnedin 1997). The value of $\Omega(z)$ can also change the properties of the density field under gravitational evolution, but this effect should be small because $\Omega(z)$ is very close to unity at high redshift. The evolution of T_0 with redshift, and the baryon fraction (Ω_b/Ω) can also affect the Jeans scale and the gravitational evolution of the photoionized gas (Gnedin & Hui 1998). These other parameters are likely to cause only small changes in observable properties compared to the five main parameters given above.

We have presented here measurements of some of the principal parameters determining the statistical properties of the Ly α forest. The mean transmitted flux determines the parameter μ , and the flux power spectrum can yield the amplitude and the effective slope of the initial mass power spectrum. We have carefully computed the error bars due to sample variance for all our results, which are generally consistent with previous ones, although the amplitude of the power spectrum is found to be slightly lower than in (Croft et al. 1999). Both the flux PDF and the power spectrum predicted in the numerical simulations in Miralda-Escudé et al. (1996) agree extremely well with what is observed. The main limitation we have for the accuracy of this comparison are the uncertainties introduced by the continuum fitting of the flux, and by the presence of narrow metal lines.

Our results for the measurement of the initial mass density perturbations are given in terms of the amplitude and power law index (i.e., the slope on a plot of $\ln P(k)$ vs. $\ln k$) of the linearly extrapolated primordial power spectrum at $k_p = 0.04 \text{ (km s}^{-1}\text{)}^{-1}$ at $z = 3$. The amplitude is $\Delta_\rho^2[k = 0.04 \text{ (km s}^{-1}\text{)}^{-1}, z = 3] = 0.72 \pm 0.09$ where $\Delta_\rho^2(k)$ is the contribution to the mass density variance per unit interval in $\ln k$. The slope is $n_p = -2.55 \pm 0.10$. This amplitude result, with its small error bar, must be thought of as partially preliminary. Further study is needed to carefully quantify the effects on the $\Delta_F^2 - \Delta_{mass}^2$ relation of changing the temperature-density relation or details of the simulations. Croft et al. (1998, 1999) found no important systematic errors but this was in the context of larger statistical error bars, and their set of simulations was not exhaustive.

If it proves to be robust, the power spectrum result can strongly constrain potential cosmological and galaxy formation models. For example, McDonald & Miralda-Escudé (1999b) found that, in order to produce the high velocities observed in studies of the kinematics of damped Ly α systems (Prochaska & Wolfe 1997, 1998), a model must obey $\sigma_{DLA4} > 0.78$ (95% confidence), where σ_{DLA4} is the linear theory rms fluctuations on spheres of radius 100 km s^{-1} at $z = 4$. The Ly α forest power spectrum amplitude we have derived in this paper implies $\sigma_{DLA4} = 0.67 \pm 0.04$, inconsistent with the above upper limit derived from damped Ly α systems at the 2.5σ level. This discrepancy, if confirmed in the future, might simply be due to a different relation between the observed velocity dispersions in damped Ly α systems and the velocity dispersions of their host dark matter halos from the one that was calculated in the spherical equilibrium models in McDonald

& Miralda-Escudé (1999b), but it should in any case provide a new constraint to understand the dynamics of damped Ly α systems.

We will also present additional results on the measurement of the parameters T_0 and γ in work that is now in preparation (P. McDonald et al. , in preparation). These parameters can be determined from the shape of the power spectrum at small scales, or by fitting absorption features to Voigt profiles and comparing the distribution of Doppler widths to what is obtained in simulations (Schaye et al. 1999; Ricotti et al. 1999; Bryan & Machacek 1999).

Apart from measuring these parameters, one should also strive to find tests for the validity of the general framework of the gravitational evolution theory in CDM models of the Ly α forest. Various perturbations from this ideal theory should be present at some level. Reionization smoothes the gas fluctuations at scales smaller than the Jeans scale for photoionized gas, but dense structures near the Jeans scale will not be ionized, heated and destroyed for a long time (Bond et al. 1988). For example, a virialized halo with velocity dispersion $\sim 10 \text{ km s}^{-1}$ should not accrete much gas when forming after reionization (since the gas has too much initial entropy and is not able to cool), but having formed before reionization it may keep its gas in thermal and hydrodynamic equilibrium, as in the minihalo model (Rees 1986; Abel & Mo 1998). These objects might introduce subtle changes in the Ly α forest that would depend on when and how the IGM was reionized. At the same time, when He II is reionized, the rapid heating of the IGM can be inhomogeneous on large scales, resulting in new fluctuations in the Ly α forest due to the gas temperature that depend on the luminosity function and spatial distribution of the ionizing sources (Miralda-Escudé & Rees 1994). Outflows from AGNs, radio sources and starbursts may also perturb the IGM at some level. Finally, the large-scale structure theory itself may be modified (for example, by having non-Gaussian primordial fluctuations). A continued effort in comparing the observed spectra with detailed numerical simulations, using a diversity of statistical probes and methods, is required to search for the influence of these phenomena.

We thank David Weinberg for his useful comments on an early draft of this paper.

A. GENERATION OF MOCK SPECTRA

To check various aspects of our data analysis procedure it is useful to have a method for creating mock spectra with properties similar to the observed ones. For example, we test our code for computing power spectra from the observations by using it to compute the known $P_F(k)$ of the mock spectra. We also test our method for generating error bars by comparing the bootstrap errors estimated from single random spectra to the ideal results obtained by generating large numbers of independent random spectra (see below).

The procedure for generating random spectra consists of the following steps:

1. Fit an analytic function to the observed $P_F(k)$.
2. Generate a Gaussian random realization of the fitted $P_F(k)$ on a large, fine grid.
3. Map the values from the grid points onto the observed pixel coordinates Δv_i .
4. Add noise to each pixel with amplitude given by the mean of the observations.

In step 1 we fit the observed $P_F(k)$ using Equation (3) multiplied by a 3D Gaussian smoothing function instead of the 1D smoothing function we generally use. We use this function because it provides a good qualitative fit to the observed $P_F(k)$ over close to the full range of k . We are not concerned with obtaining the best possible fit because we only want to generate mock spectra with a precisely *known* input power spectrum that will have properties similar to the observed one. In step 2 we generate a Gaussian random field with Fourier mode amplitudes given by $\langle a_k^2 \rangle = P_F(k)$ where $P_F(k)$ is given by the fitting formula from step 1. The grid used is evenly spaced in velocity and is always longer than the observed spectrum by a factor of at least 8 with resolution better by a factor of at least 4. In step 3 we superimpose the uneven set of observed pixel locations on top of the grid generated in step 2 (using a random origin). The value of F_i assigned to each Δv_i is linearly interpolated from the two adjacent values on the fine grid. The spectra generated by this procedure do not have identical statistics to the observations because the observations are not Gaussian but this should not be important for our purposes.

Although the random fields that we generate have the same power spectrum as the observed spectra, they have a Gaussian PDF which is not limited to the range $0 < F < 1$. It should be possible to create more realistic spectra by generating a Gaussian (or even non-Gaussian) field for the optical depth or the baryon density instead of the transmitted flux (e.g., Bi 1993). We have adopted the very simple method of generating a Gaussian field and calling it the transmitted flux because this allows us to use directly the power spectrum measured from the observed transmitted flux.

B. BOOTSTRAP ERROR BARS

It is well known that gravitational collapse leads to non-Gaussianity of the density field in the non-linear regime probed by the smallest scales in the Ly α forest. It is generally difficult to estimate error bars on measurements when we cannot assume that the underlying process is Gaussian. To solve this problem we compute error bars for all of the numbers measured in this paper using a variation of the bootstrap method (Press et al. 1992).

If we have N independent data segments, a bootstrap realization of a computed statistic is created by randomly drawing N segments from the set with replacement and recomputing the statistic from the randomly modified set of data. The bootstrap error bar on a statistic is simply the dispersion among the bootstrap realizations of the statistic. Ideally we would like to divide the data sample into numerous independent parts with identical statistical properties as we could if we had a large number of quasars all at the same redshift for example. Unfortunately we only have

8 quasars and no more than 5 in a single redshift bin. One would think that because the spectra are long relative to the correlation length they can be split into some number of approximately independent chunks and the bootstrap method applied to those chunks. The question then is how large must these chunks be relative to the correlation length? We can analytically investigate the applicability of the bootstrap method for the situation at hand in the special case where we assume the field *is* Gaussian. The bootstrap method does not depend on the field being Gaussian so we can hope that if it works in the Gaussian case it will work similarly well on observational data with the same power spectrum.

We now investigate analytically the requirements for obtaining reliable bootstrap errors in the case where we are segmenting correlated data. We represent an abstract set of data by δ_i where $i = 1..N$ runs over all N pixels. To make analytic calculations possible we assume δ is a Gaussian random field with $\langle \delta \rangle = 0$, $\langle \delta^2 \rangle = \sigma^2 = \xi(0)$, and $\langle \delta_i \delta_j \rangle = \xi(i - j)$. We want to imagine the situation where the data has been split into N/c segments each containing c pixels. If f is some statistic that can be measured from the data (like the mean), we define \tilde{f} to be the value of f that is actually computed from a given set of data, and $\tilde{\tilde{f}}$ to be the value of f computed from a bootstrap realization of the same data used to compute \tilde{f} . Taking the variance as an example we have

$$\tilde{\sigma}^2 = \frac{1}{N} \sum_{i=1}^N \delta_i^2 \quad (\text{B1})$$

and

$$\tilde{\tilde{\sigma}}^2 = \frac{1}{N} \sum_{s=0}^{\frac{N}{c}-1} o_s \sum_{i=sc+1}^{sc+c} \delta_i^2 \quad (\text{B2})$$

where o_s is the number of times that data segment s was drawn in forming the bootstrap realization. The occupation numbers o_i have the following property

$$\langle (o_i - 1)(o_j - 1) \rangle_b = \delta_{ij} \left(\frac{N_s}{N_s - 1} \right) - \frac{1}{N_s - 1} \quad (\text{B3})$$

where $\langle \rangle_b$ represents an average over different bootstrap realizations of the same data, $N_s \equiv N/c$ is the number of segments drawn from, and $\delta_{ij} = 1$ for $i = j$ and $\delta_{ij} = 0$ for $i \neq j$. We will generally use the large N_s approximation

$$\langle (o_i - 1)(o_j - 1) \rangle_b = \delta_{ij} - \frac{1}{N_s} . \quad (\text{B4})$$

To demonstrate the application of this formalism we will compute the bootstrap error on $\tilde{\sigma}^2$. To make the algebra more transparent we will further simplify the calculation by making the assumption that the pixels are uncorrelated and the segment length is only one pixel:

$$\left\langle \left(\tilde{\sigma}^2 - \tilde{\tilde{\sigma}}^2 \right)^2 \right\rangle_b = \left\langle \left(\frac{1}{N} \sum_{i=1}^N (o_i - 1) \delta_i^2 \right)^2 \right\rangle_b . \quad (\text{B5})$$

Evaluating the expectation value over bootstrap realizations gives

$$\left\langle \left\langle \left(\tilde{\sigma}^2 - \sigma^2 \right)^2 \right\rangle_b \right\rangle = \frac{1}{N^2} \sum_{i=1}^N \delta_i^2 \sum_{i'=1}^N \delta_{i'}^2 \left(\delta_{ii'} - \frac{1}{N} \right) . \quad (\text{B6})$$

In this simplified case it is easy to find the true error on σ^2 from the assumption that the field is Gaussian. The result is

$$\left\langle \left\langle \left(\tilde{\sigma}^2 - \sigma^2 \right)^2 \right\rangle \right\rangle = \frac{2\sigma^4}{N} . \quad (\text{B7})$$

To relate this to the bootstrap error we must take the expectation value of Equation (B6) over different realizations of the underlying Gaussian distribution to obtain

$$\left\langle \left\langle \left\langle \left(\tilde{\sigma}^2 - \sigma^2 \right)^2 \right\rangle_b \right\rangle \right\rangle = \frac{1}{N^2} \sum_i 3\sigma^4 - \frac{1}{N^3} \sum_i \sum_j (\sigma^4 + 2\sigma^4 \delta_{ij}) = \frac{2\sigma^4}{N} \quad (\text{B8})$$

where we have completed all of the sums using $\langle \delta_i \delta_j \rangle = \xi(i-j) = \delta_{ij}$ and dropped terms of higher order in N^{-1} . We see that the correct result is obtained in the large N limit.

The error on the correlation function is more complicated and we will not assume uncorrelated pixels or one-pixel segments. The exact result for a Gaussian field in the limit that the data set is much longer than the correlation length is

$$\left\langle \left\langle \left(\tilde{\xi}_n - \xi_n \right) \left(\tilde{\xi}_m - \xi_m \right) \right\rangle \right\rangle = \frac{1}{N} \sum_{k=-N}^N (\xi_k \xi_{k+n-m} + \xi_{k-m} \xi_{k+n}) \quad (\text{B9})$$

where we have also assumed that n and m are much smaller than the length of the data set. A bootstrap realization of ξ is given by

$$\tilde{\xi}_n = \frac{1}{N} \sum_{s=0}^{\frac{N}{c}-1} o_s \sum_{i=sc+1}^{sc+c} \delta_i \delta_{i+n} . \quad (\text{B10})$$

After evaluating the bootstrap average we find

$$\left\langle \left\langle \left\langle \left(\tilde{\xi}_n - \xi_n \right) \left(\tilde{\xi}_m - \xi_m \right) \right\rangle_b \right\rangle \right\rangle = \frac{1}{N^2} \sum_{s=0}^{\frac{N}{c}-1} \sum_{s'=0}^{\frac{N}{c}-1} \sum_{i=sc+1}^{sc+c} \sum_{i'=s'c+1}^{s'c+c} \delta_i \delta_{i+n} \delta_j \delta_{j+m} \left(\delta_{ss'} - \frac{c}{N} \right) . \quad (\text{B11})$$

If we make the assumption that the data set is long enough that it can be split into many segments with each segment much longer than the correlation length the calculation of the bootstrap errors averaged over realizations of the Gaussian field gives the correct result:

$$\left\langle \left\langle \left\langle \left(\tilde{\xi}_n - \xi_n \right) \left(\tilde{\xi}_m - \xi_m \right) \right\rangle_b \right\rangle \right\rangle = \frac{1}{N} \sum_{k=-c}^c (\xi_k \xi_{k+n-m} + \xi_{k-m} \xi_{k+n}) . \quad (\text{B12})$$

The assumptions we were forced to make so that the bootstrap error came out correct seem to be the ones that would be expected intuitively: the data set must be split into a large number of

segments and those segments must be larger than the correlation length of the data. Note that cross correlations for widely separated n and m will not be accurately reproduced but only if they are so widely separated that the cross correlation is in fact very small. We have really only shown that the bootstrap method can be made to work in the infinite data limit.

To investigate the effectiveness of the bootstrap method applied to real data we turn to the mock spectra described in Appendix A. We generate a set of 50 of each quasar spectrum and apply the data analysis procedure to them exactly as we have done with the observational data. We find that the optimal number of segments for our redshift bins seems to be about 300 giving segments approximately 100 pixels long. The errors on σ_F^2 , the PDF, and $\xi(\Delta v)$ are underestimated by 5-15% for the three redshift bins using this size segments. The error estimated for the mean transmitted flux seems to be more strongly affected by the long range correlations (underestimated by a factor of 1.6 in the worst case), probably because it is only first order in ξ instead of second order like we see in Equation (B9).

To correct for these underestimations we find the ratio of the true error to the bootstrap error in the mock spectra for every statistic we measure and then multiply the bootstrap error on the observational measurement by this factor. In the case of the PDF and correlation function we have a full error matrix including the correlations between errors on different bins. We judge the underestimation of the errors by looking at χ^2 tests comparing the PDF or ξ for all possible pairs of mock data sets. The mean value of χ^2/ν for ν degrees of freedom should be 1 and the full distribution of χ^2 can be computed easily. We find that the mean χ^2 computed using the bootstrap errors is no more than 20% higher than expected and we rescale the error matrix of the observational data by this overall factor instead of trying to correct the individual matrix elements. With this rescaling the distribution of χ^2 becomes essentially perfect. Note that we do not in any way compute the observational errors from the Gaussian mock spectra since we use them only to find edge effect corrections that are then applied to the bootstrap errors calculated from the observational data.

Although it plays a large part in the paper, in this discussion we have left out any mention of the power spectrum. We have not found a fully satisfactory method for computing a full error matrix for $P_F(k)$ using the bootstrap method. We do not get correct results using the type of analytic calculations we did for the correlation function. This is probably because we need to treat the edge effects from the finite data set more carefully in the case of the power spectrum. The obvious technical problem with simply applying the method to the data anyway is that we can not make the segments very small and still measure the power spectrum from them. We need to keep the segments a few times larger than the longest wavelength for which we want to measure $P(k)$ but this restricts the number of them for our data set to about 10. We have tried computing full error matrices for our mock spectra using only 10 segments but the results are discouraging. The distribution of χ^2 computed from these matrices is not close to what is expected. This is because the statistical error in estimating all of the error matrix elements from only ten segments is too high. Note that in our mock spectra there are *no* correlations between the $P_F(k)$ bins so any

that we find in the bootstrap realizations are simply noise. Visually comparing the error matrices from the mock spectra and the real data we find that they look very similar. There is no obvious evidence that the errors in the real data are more correlated than the theoretically uncorrelated mock data (both become strongly correlated at very high k where the window function becomes important). We will simply use the diagonal elements of the bootstrap error matrix and treat the bin errors as independent. We correct the errors on each bin separately by comparing the true and bootstrap errors in the mock spectra. These corrections are only significant ($\sim 30\%$) on the longest wavelength modes. Note that using independent bootstrap errors on each bin still takes into account the correlation between the individual k modes that are averaged to give the bin value. The measurement of the amplitude shows that at the redshifts in question the modes with $k < 0.04 \text{ (km s}^{-1}\text{)}^{-1}$ should not be fully non-linear supporting the supposition that the correlations between bins is not large.

C. THE $\text{Ly}\alpha$ FOREST FLUX POWER SPECTRUM IN THE LARGE SCALE LIMIT

This Appendix shows that the flux power spectrum in the $\text{Ly}\alpha$ forest must indeed be proportional to the mass power spectrum in the limit of large scales, as was first assumed by citet{cwk98}. We shall first consider the simple case where the effect of peculiar velocities is neglected.

Let $P_0(F)$ be the flux probability distribution, and $P(F|\bar{\delta})$ be the conditional distribution of F given that the overdensity smoothed over a certain scale R_s around the point where the flux F is observed is $\bar{\delta}$. We consider the correlation of the transmitted flux at two points, F_1 and F_2 , separated by a distance much larger than R_s , but where R_s is still a sufficiently large scale for linear theory to be valid. In this case, the correlation of F_1 and F_2 should be exclusively due to the correlation of $\bar{\delta}_1$ and $\bar{\delta}_2$, the smoothed densities around the points 1 and 2. In other words, the joint probability distribution $P_2(F_1, F_2)$ should be equal to the product $P(F_1|\bar{\delta}_1)P(F_2|\bar{\delta}_2)$ (notice that the correlation of the whole deformation tensor at the two points should enter here at the same order as the density correlation; we are assuming that the constrained probability distribution of the flux depends mostly on the overdensity, and not the other components of the deformation tensor). Since $\bar{\delta} \ll 1$, we can write $P(F|\bar{\delta}) = P_0(F) + \bar{\delta} P_\delta(F)$, where $P_\delta(F) = [dP(F|\bar{\delta})/d\bar{\delta}]_{\bar{\delta}=0}$. The flux correlation function is then given by:

$$\begin{aligned} \langle F_1 F_2 \rangle &= \int dF_1 dF_2 \langle [P_0(F_1) + \bar{\delta}_1 P_\delta(F_1)] [P_0(F_2) + \bar{\delta}_2 P_\delta(F_2)] F_1 F_2 \rangle \\ &= \langle \bar{\delta}_1 \bar{\delta}_2 \rangle \int dF_1 dF_2 P_\delta(F_1) P_\delta(F_2) F_1 F_2 \\ &= \xi(x_{12}) \cdot \left[\int dF P_\delta(F) F \right]^2 \end{aligned}$$

$$= \xi(x_{12}) \cdot \left(\frac{d\bar{F}}{d\bar{\delta}} \right)^2, \quad (\text{C1})$$

where $\xi(x_{12}) = \langle \bar{\delta}_1 \bar{\delta}_2 \rangle$ is the density correlation function at the separation x_{12} between points 1 and 2, and $\bar{F}(\bar{\delta}) = \int dF F P(F, \bar{\delta})$. This gives an expression for the B factor defined in §5.7.

When peculiar velocities are included, there should be an additional dependence of $P(F)$ on the peculiar velocity gradient along the line of sight, $\eta = H^{-1} dv_p/dl$ (where d/dl is the derivative along the line of sight), averaged over the same scale R_s . We can linearize as before $P(F, \bar{\delta}, \bar{\eta}) = P_0(F) + \bar{\delta} P_\delta(F) + \bar{\eta} P_\eta(F)$, and define the factor

$$b_F = \left(\int dF P_\delta(F) F \right) / \left(\int dF P_\eta(F) F \right). \quad (\text{C2})$$

The quantity b_F is a different “bias factor” for the Ly α forest, this one intended for peculiar velocity calculations. Defining the new variable $\bar{\delta}_z = \bar{\delta} + b_F^{-1} \bar{\eta}$, we obtain

$$\langle F_1 F_2 \rangle = \xi_z(x_{12}) \cdot \left(\frac{\partial \bar{F}}{\partial \bar{\delta}} \right)^2, \quad (\text{C3})$$

where ξ_z is the redshift space correlation function along the line of sight of δ_z , which has bias factor b_F . Thus, we see that both b_F and $B = \partial \bar{F} / \partial \bar{\delta}$ are functions of the flux distribution $P_0(F)$, and of how this distribution varies with the overdensity and the peculiar velocity gradient smoothed over a large scale around the point where the flux is being measured. This implies a complex dependence of b_F and B on all the variables determining the Ly α forest properties, such as the fluctuation amplitude on the Jeans scale, the mean transmitted flux, and the temperature-density relation.

REFERENCES

- Abel, T. & Mo, H. J. 1998, ApJ, 494, L151
- Arons, J. 1972, ApJ, 172, 553
- Bahcall, J. N. & Salpeter, E. E. 1965, ApJ, 142, 1677
- Bardeen, J. M., Bond, J. R., Kaiser, N., & Szalay, A. S. 1986, ApJ, 304, 15
- Barlow, T. A., & Sargent, W. L. W. 1997, AJ, 113, 136
- Bechtold, J., Crofts, A. P. S., Duncan, R. C., & Fang, Y. 1994, ApJ, 437, L83
- Bi, H. 1993, ApJ, 405, 479
- Bond, J. R., Szalay, A. S., & Silk, J. 1988, ApJ, 324, 627
- Bryan, G. L., & Machacek, M. E. 1999, ApJ, submitted (astro-ph/9906459)

- Burles, S. & Tytler, D. 1998, *ApJ*, 499, 699
- Cen, R., Miralda-Escudé, J., Ostriker, J. P., & Rauch, M. 1994, *ApJ*, 437, L9
- Croft, R. A. C., Hu, W., & Davé, R. 1999, *Phys. Rev. Lett.*, 83, 1092
- Croft, R. A. C., Weinberg, D. H., Katz, N., & Hernquist, L. 1998, *ApJ*, 495, 44
- Croft, R. A. C., Weinberg, D. H., Pettini, M., Hernquist, L., & Katz, N. 1999, *ApJ*, 520, 1
- Crotts, A. P. S., & Fang, Y. 1998, *ApJ*, 502, 16
- Dinshaw, N., Impey, C. D., Foltz, C. B., Weymann, R. J., & Chaffee, F. H. 1994, *ApJ*, 437, L87
- Gnedin, N. Y., & Hui, L. 1998, *MNRAS*, 296, 44
- Hernquist, L., Katz, N., Weinberg, D. H., & Miralda-Escudé, J. 1996, *ApJ*, 457, L51
- Hui, L., & Gnedin, N. Y. 1997, *MNRAS*, 292, 27
- Hui, L. 1999, *ApJ*, 516, 519
- Jenkins, E. B., & Ostriker, J. P. 1991, *ApJ*, 376, 33
- Ma, C. 1996, *ApJ*, 471, 13
- McDonald, P., & Miralda-Escudé, J. 1999a, *ApJ*, 518, 24
- McDonald, P., & Miralda-Escudé, J. 1999b, *ApJ*, 519, 486
- McGill, C. 1990, *MNRAS*, 242, 544
- Miralda-Escudé, J., Cen, R., Ostriker, J. P., & Rauch, M. 1996, *ApJ*, 471, 582
- Miralda-Escudé, J., & Rees, M. J. 1993, *MNRAS*, 260, 617
- Miralda-Escudé, J., & Rees, M. J. 1994, *MNRAS*, 266, 343
- Nusser, A., & Haehnelt, M. 1999, *MNRAS*, 303, 179
- Press, W., Teukolsky, S., Vetterling, W., & Flannery, B. 1992, *Numerical Recipes in C* (2d ed.; Cambridge:Cambridge University Press)
- Press, W. H., Rybicki, G. B., & Schneider, D. P. 1993, *ApJ*, 414, 64
- Prochaska, J. X., & Wolfe, A. M. 1997, *ApJ*, 487, 73
- Prochaska, J. X., & Wolfe, A. M. 1998, *ApJ*, 507, 113
- Rauch, M., Miralda-Escudé, J., Sargent, W. L. W., Barlow, T. A., Weinberg, D. H., Hernquist, L., Katz, N., Cen, R., & Ostriker, J. P. 1997, *ApJ*, 489, 7

- Rauch, M. 1998, *ARA&A*, 36, 267
- Rauch, M., Carswell, R. F., Chaffee, F. H., Foltz, C. B., Webb, J. K., Weymann, R. J., Bechtold, J., & Green, R. F. 1992, *ApJ*, 390, 387
- Rees, M. J. 1986, *MNRAS*, 218, 25P
- Ricotti, M., Gnedin, N. Y., & Shull, J. M. 1999, *ApJ*, submitted (astro-ph/9906413)
- Schaye, J., Theuns, T., Leonard, A., Efstathiou, G. 1999, *MNRAS*, in press (astro-ph/9906271)
- Scherrer, R. J., & Weinberg, D. H. 1998, *ApJ*, 504, 607
- Smette, A., Surdej, J., Shaver, P. A., Foltz, C. B., Chaffee, F. H., Weymann, R. J., Williams, R. E., & Magain, P. 1992, *ApJ*, 389, 39
- Smette, A., Robertson, J. G., Shaver, P. A., Reimers, D., Wisotzki, L., & Köhler, Th. 1995, *A&AS*, 113, 199
- Theuns, T., Leonard, A., Efstathiou, G., Pearce, F. R., & Thomas, P. A. 1998, *MNRAS*, 301, 478
- Vogt, S. S., et al. 1994, *SPIE* 2198, 362
- Wadsley, J. W., & Bond, J. R. 1996, preprint, (astro-ph/9612148)
- Wang, L., Caldwell, R. R., Ostriker, J. P., & Steinhardt, P. J. 1999, *ApJ*, in press (astro-ph/9901388)
- Weinberg, D. H., Miralda-Escudé, J., Hernquist, L., & Katz, N. 1997, *ApJ*, 490, 564
- Weinberg, D. H., Croft, R. A. C., Hernquist, L., Katz, N., & Pettini, M. 1999, *ApJ*, 522, 563
- Zhang, Y., Anninos, P., & Norman, M. L. 1995, *ApJ*, 453, L57
- Zhang, Y., Anninos, P., Norman, M. L., & Meiksin, A. 1997, *ApJ*, 485, 496